Nanophysiology Approach Reveals Diversity in Calcium Microdomains in Zebrafish Retinal Bipolar Ribbon Synapses

Nirujan Rameshkumar[1*], Abhishek P Shrestha[1*#], Johane M. Boff[1*], Mrinalini Hoon[2,3,4], Victor Matveev[5], David Zenisek [6,7], Thirumalini Vaithianathan[1,8 $]

[1] Department of Pharmacology, Addiction Science, and Toxicology, The University of Tennessee Health Science Center, TN 38163.

[2] Department of Neuroscience, University of Wisconsin, Madison, WI, USA.

[3] McPherson Eye Research Institute, University of Wisconsin, Madison, WI, USA.

[4] Department of Ophthalmology and Visual Sciences, University of Wisconsin, Madison, WI, USA.

[5] Department of Mathematical Sciences, New Jersey Institute of Technology, Newark, NJ 07102, USA.

[6] Department of Cellular and Molecular Physiology, Yale University School of Medicine, New Haven, CT 06520-8066, USA.

[7] Department of Ophthalmology and Visual Sciences, Yale University School of Medicine, New Haven, CT 06520-8066, USA.

[8] Department of Ophthalmology, Hamilton Eye Institute, University of Tennessee Health Science Center, Memphis, TN 38163, USA.

* These authors contributed equally to this work.

[#] Current Address: Department of Surgery, College of Medicine, University of Florida, Gainesville, Florida.

[$] Contact: Thirumalini Vaithianathan, Ph.D., tvaithia@uthsc.edu.

Abstract

Rapid and high local calcium (Ca^{2+}) signals are essential for triggering neurotransmitter release from presynaptic terminals. In specialized bipolar ribbon synapses in the retina, these local Ca^{2+} signals control multiple processes, including the priming, docking, and translocation of vesicles on the ribbon before exocytosis and the replenishment of release-ready vesicles to the fusion sites to sustain neurotransmission. However, our knowledge about Ca^{2+} signals along the axis of the ribbon active zone is limited. Here, we used fast confocal quantitative dual-color ratiometric line-scan imaging of a fluorescently labeled ribbon binding peptide and Ca^{2+} indicators to monitor the spatial and temporal aspects of Ca^{2+} transients of individual ribbon active zones in zebrafish retinal rod bipolar cells. We observed that a Ca^{2+} transient elicited a much greater fluorescence amplitude when the Ca^{2+} indicator was conjugated to a ribeye-binding peptide than when using a soluble Ca^{2+} indicator, and the estimated Ca^{2+} levels at the ribbon active zone exceeded 26 μM in response to a 10-millisecond stimulus, as measured by a ribbon-bound low-affinity Ca^{2+} indicator. Our quantitative modeling of Ca^{2+} diffusion and buffering is consistent with this estimate and provides a detailed view of the spatiotemporal [Ca^{2+}] dynamics near the ribbon. Importantly, our data demonstrates that the local Ca^{2+} levels may vary between ribbons of different rod bipolar cells and within the same cells. The variation in local Ca^{2+} signals is likely due to heterogeneity in local Ca^{2+} channels clustered at the ribbon active zone, as serial electron microscopy provides new information about the heterogeneity in ribbon size, shape, and area of the ribbon in contact with the plasma membrane.

Introduction

Sensory synapses in the retina rely on the proper function of a specialized organelle, the synaptic ribbon [1-5]. Retinal bipolar cells (BPCs) serve as the major conduit for transmitting visual information across the vertebrate retina. Rod BPCs can release brief bursts of neurotransmitters to signal a change in contrast or sustain the continuous release of neurotransmitters in a graded manner to provide an analog read-out of luminance [6]. To maintain this ability, the BPCs must exert dynamic control over neurotransmitter release rate and facilitate efficient recruitment of release-ready vesicles to fusion sites on the synaptic ribbon. It has been established that the elevation of presynaptic Ca^{2+} in rod BPCs both regulates dynamic changes in the release rate and accelerates the rate of vesicle replacement [6-14]. However, the spatiotemporal properties of the Ca^{2+} signals that control neurotransmitter release and the molecular entities that regulate the interplay between these Ca^{2+} signals and synaptic vesicle dynamics to sustain kinetically distinct neurotransmitter release components remain poorly understood. Here, we sought to address this lack of knowledge by measuring local Ca^{2+} signals at positions along the synaptic ribbon at different distances from the cytomatrix at the active zone (CAZ) in retinal rod BPCs isolated from zebrafish.

Resolving local Ca^{2+} signals is technically challenging as it requires information about the spatiotemporal properties of Ca^{2+} signals specific to ribbon sites. Previous studies of Ca^{2+} dynamics in rod BPCs focused primarily on the terminal as a whole and used quantitative methods to examine bulk Ca^{2+} levels, which are significantly lower and slower than those occurring at the active zone [15-18]. We showed that the Ca^{2+} signals at a single ribbon active zone in rod bipolar cells likely exceed 10μM within 3 milliseconds after the opening of the Ca^{2+} channels [19]. However, these studies were largely focused on estimating the Ca^{2+} signals at the plasma membrane that drive fast, transient neurotransmitter release, rather than measurements of Ca^{2+} signals along the axis of ribbon, which are the signals that actually control trafficking and priming of vesicles for slower phases of release. To address this question, we establish a nanophysiology ratiometric approach that measures the spatial and temporal properties of Ca^{2+} transients by targeting the Ca^{2+} indicator to the ribbon via conjugation to a ribbon binding peptide (RBP) [20]. The average local Ca^{2+} levels measured with a ribbon-bound low-affinity Ca^{2+} indicator was approximately 26.4 ± 3.1 μM in ribbon locations proximal to the plasma membrane and 15.6 ± 1.5 μM on the distal portion of the ribbon. Resolving Ca^{2+} signals associated within the sub-diffraction sized domains within the CAZ is impossible due to the finite spatiotemporal resolution of optical

imaging. Thus, we employed a quantitative model using Ca^{2+} diffusion and buffering to resolve the Ca^{2+} signals associated with CAZ and along the ribbon and provide a detailed description of the spatiotemporal Ca^{2+} dynamics.

Our nanophysiology approach to measuring local Ca^{2+} transients at a single ribbon with high spatiotemporal resolution provides the first evidence of heterogeneity of Ca^{2+} signals at rod bipolar ribbon synapses. Previous studies on sensory synapses have reported heterogeneity in the amplitude of ribbon-localized Ca^{2+} signals in the synaptic ribbons of salamander cone photoreceptors[21] and mouse inner hair cells, [22,23] suggesting that this variability contributes to diversification in transmitter release rates. Additionally, differences in local Ca^{2+} influx or subunit composition of Ca^{2+} channels have also been reported in hippocampal synapses.[24] The heterogeneity in local Ca^{2+} signals we found at some ribbons from the same cell or across different retinal BPC), may arise from distinct mechanisms. The faster, smaller, and more spatially confined Ca^{2+} signals that are insensitive to the application of high concentrations of exogenous Ca^{2+} buffers, referred to here as ribbon proximal Ca^{2+} signals, could be due to Ca^{2+} influx through Ca^{2+} channel clusters beneath the synaptic ribbon. However, the variability in Ca^{2+} signals at the distal ribbon, away from the plasma membrane, may result from the spread between two closely spaced microdomains; thus, if proximal Ca^{2+} signals are variable, the distal Ca^{2+} signals are also variable between ribbons. Alternatively, the variability in distal Ca^{2+} signals could be due to additional mechanisms, for example, Ca^{2+} influx from internal stores. In the current study, we investigated the possible mechanisms for heterogeneity in proximal Ca^{2+} signals by measuring the ribbon size, particularly the area of the ribbon adjacent to the plasma membrane, where Ca^{2+} channel clusters are located. Serial block-face scanning electron microscopy (SBF-SEM) shows substantial variability in synaptic ribbon size, shape, and the area of the ribbon facing the plasma membrane where Ca^{2+} channel clusters are tethered. Since both Ca^{2+} signals and the area of the synaptic ribbon facing the plasma membrane are heterogeneous, we propose that the larger ribbons may anchor more channels, leading to larger Ca^{2+} microdomains. Since local Ca^{2+} signals control kinetically distinct neurotransmitter release components, heterogeneity in local Ca^{2+} signals may alter the rate of vesicle release and allow them to function independently. Our nanophysiology approach reveals diversity in Ca^{2+} signals at rod bipolar ribbon synapses, which may increase the dynamic range of rod bipolar ribbon synapses [25-27], as discussed previously for hair cells and cone ribbon synapses [21-23,28,29].

Results

Quantitative nanophysiology approach reveals spatiotemporal properties of local Ca^{2+} signals in zebrafish retinal bipolar cell terminals.

The flow used in our quantitative nanophysiology approach to measure local Ca^{2+} signals at individual ribbon active zones is shown in **Fig.1**. Fluorescently labeled ribeye binding peptide (RBP) [30] and high affinity Ca^{2+} indicator Cal-520® (Cal520HA, K_D 320 nM) were delivered to rod BPC via a whole-cell patch pipette placed directly at the cell terminal. Rapid x-t line scans at the ribbon location were performed to localize synaptic ribbons (**Fig.1A a2**) and to monitor local changes in Ca^{2+} concentration at a single ribbon, as we demonstrated previously to estimate the Ca^{2+} levels at the plasma membrane and to track a single synaptic vesicle at ribbon locations [19,20]. The z-projection from a series of confocal optical sections through the synaptic terminal (**Fig. 1A a1**) illustrates ribbon labeling (magenta spots). RBP fluorescence was used to localize a synaptic ribbon and to define a region for placing a scan line perpendicular to the plasma membrane, extending from the extracellular space to the cytoplasmic region beyond the ribbon to monitor changes in the Ca^{2+} concentration along the ribbon axis (**Fig. 1A a2**). Sequential dual laser scanning was performed at rates of 1.51 millisecond per line. The spatial resolution was limited by the point spread function (PSF) of the microscope to an x- and y-width of 268 and 273 nm, respectively (**Supplementary Fig.1**).

Two-color laser scanning methods allowed observation of Ca^{2+} signals throughout the full extent of the ribbon in voltage-clamped synaptic terminals, while the ribbon and cell border were imaged with a second fluorescent label. Exchange of TTL (transistor-transistor logic) pulses between the patch-clamp and imaging computers synchronized the acquisition of electrophysiological and imaging data. The precise timing of imaging relative to voltage-clamp stimuli was established using PatchMaster software to digitize horizontal-scan synced pulses from the imaging computer in parallel with the electrophysiological data (**Fig.1B**). In our previous studies, line scans have been applied primarily to the measurement of the temporal properties of Ca^{2+} signals [19]. However, x-t raster plots obtained at a ribbon active zone labeled with RBP can also be used to derive the spatial profile (**Fig.1C**) in addition to the temporal aspects (**Fig.1D**) of Ca^{2+} transients relative to the synaptic ribbon and plasma membrane, as we previously described [31].

To determine the Ca^{2+} signals along the ribbon axis, we spatially averaged the x-axis profile intensity of RBP (i.e., a horizontal row of pixels, see **Fig.1C, *top***) to determine the position of the center of the ribbon and estimate the location of the plasma membrane (see Materials and Methods). The parameter x_0 is the peak of the Gaussian fit, giving the x-position of the center of the ribbon (see Materials and Methods). The x-axis profile is also used to obtain the spatial profile of Ca^{2+} signals before, during, and after with respect to the ribbon profile. **Fig.1C**, bottom, demonstrates that the peak of the Ca^{2+} signals (x_0, cyan; **Fig.1C**) during the stimuli is proximal to the ribbon center (x_0, magenta; **Fig.1C**) towards the plasma membrane ($x_{1/2}$, magenta; **Fig.1C**), as expected for Ca^{2+} influx originating from Ca^{2+} channels localized in the plasma membrane [32-34]. **Fig.1D** shows an example of the temporal profile of Ca^{2+} signals at the ribbon shown in **Fig.1C** : during the stimulus, fluorescence rose rapidly, and after depolarization terminated, Ca^{2+} current rapidly deactivated (see also **Fig.1B**, black), and Cal520HA fluorescence at the ribbon showed a rapid decrease in fluorescence followed by a slower decrease to the baseline, with a time constants of 8 and 114 milliseconds respectively. Capacitance measurements (**Fig.1B**, blue) were used to determine overall synaptic dynamics. Collectively, this novel imaging approach allowed us to simultaneously 1) determine the kinetics and Ca^{2+} signal gradient along the synaptic ribbon, 2) compare local Ca^{2+} signals at different ribbons within a single BPC terminal, 3) inform a model to estimate the Ca^{2+} concentrations along the ribbon that control distinct neurotransmitter release, 4) measure Ca^{2+} concentrations during depolarization at single ribbon locations, 5) measure exocytosis efficiency, and 6) reveal exogeneous buffering effects on local Ca^{2+} signals as described below.

Heterogeneity in local Ca^{2+} signals at a single ribbon active zone of rod BPC.

Synaptic vesicles in rod BPCs are distributed among at least four distinct pools based on their fusion kinetics, the average proximity of vesicles to Ca^{2+} channels, and the state of vesicle preparedness for Ca^{2+}-triggered fusion [1,6,8,11-13,27,35-38]. All the vesicles in the ribbon are molecularly prepared for fusion but differ in their anatomical distance to Ca^{2+} channels at the plasma membrane, leading to a clear kinetic distinction between the first and second phases of exocytosis triggered by strong activation of the Ca^{2+} current. The ultrafast releasable pool (UFRP) is comprised of RRP vesicles that are docked at the base of the synaptic ribbon [11] , as shown in **Supplementary Fig. 2** (green vesicles), which participate in the first, most rapid phase of exocytosis. The remaining RRP vesicles were localized to the portion of the ribbon that is distal to the plasma membrane

(**Supplementary Fig. 2**; yellow vesicles), which are believed to contribute to the second, slower phase of neurotransmitter release [11,12,37,39,40]. The ribbon pools are replenished by vesicles in the cytoplasmic recycling pool (RP; **Supplementary Fig. 2,** orange vesicles), and vesicles that do not participate in neurotransmitter release are known as reserved pools (Res. P; **Supplementary Fig. 2,** blue vesicles).

First, we examined the dynamics of local Ca^{2+} signals that control the transient components of the UFRP and RRP using soluble Ca^{2+} indicators in response to 10ms brief stimuli. We used the higher affinity Cal520HA (effective Kd = 795 nM; see methods) to obtain smaller changes in the Ca^{2+} signals in response to brief stimuli. We performed whole-cell voltage-clamped recordings by placing the patch pipette filled with Cal520HA and TAMRA-RBP at the rod BPC terminal and waited 30 s after break-in to allow Cal520HA to reach equilibrium with the patch-pipette before obtaining the first fluorescent image (**Supplementary Fig 3A**). We analyzed individual x-t raster plots (**Fig. 2A**) of TAMRA-RBP (magenta) and Cal520HA (Cyan) to determine the spatial (horizontal x-axis) (**Fig. 2B**) and temporal (vertical t-axis) profiles of Cal520HA fluorescence intensity relative to the position of the synaptic ribbon (**Fig. 2C**). The spatial profile of Ca^{2+} signals before (**Fig. 2B**, black lines), during (**Fig. 2B**, cyan line), and after depolarization (**Fig. 2B**, gray line) demonstrated the overall changes in Ca^{2+} signals at a ribbon location (**Fig. 2B**, magenta) in response to the stimulus. To measure the temporal Ca^{2+} profile at different distances from the plasma membrane, we analyzed x-t line scan analysis along the time-axis at distinct distances (**Fig. 2C**) based on the spatial profile of the ribbon as described in **Fig.1C**. At the onset of the stimulus (**Fig. 2A b,** white arrowhead and **Fig. 2C**, black arrow), the fluorescence at the ribbon-proximal location rose most rapidly and to a higher level (**Fig. 2C** red trace) than that at the cytoplasmic location (**Fig. 2Ab,** white arrow and **Fig. 2C,** green trace), indicating that the locus of Ca^{2+} influx was proximal to the membrane relative to the ribbon center. The rise time, defined here as the time to reach half-maximal peak fluorescence amplitude from the resting amplitude is faster for the proximal (~2.81 millisecond) than distal (~3.44 millisecond) and cytoplasmic (~6.14 millisecond) signals, with the distal being faster than the cytoplasmic. The maximum value of, $\Delta F/F_{rest}$ (changes in the fluorescence during depolarization normalized to before depolarization) achieved from the average Ca^{2+} transients obtained using Cal520HA at proximal, distal, and cytoplasmic locations were 1.9 ± 0.3, 1.5 ± 0.25, and 1 ± 0.15 (mean ± SEM), respectively (**Fig. 2C**). As expected, the amplitude of the proximal Ca^{2+} signals (i.e., those nearest the Ca^{2+} channel locations) measured with Cal520HA was different from that of the cytoplasmic Ca^{2+} signals (p<

0.001, N=24; 95% confidence limit) and the proximal Ca^{2+} signals differed significantly from those of the distal signals ($p< 0.001$, N=24; 95% confidence limit). These findings suggest that our spatial resolution, using Cal520HA, is sufficient to distinguish differences in the Ca^{2+} signals within 300 nm.

Notably, we found that the local Ca^{2+} signals at the ribbon location varied between cells, primarily in the amplitude of the Ca^{2+} transients, even in BPCs with similar currents (**Fig. 2Da** vs. **Fig 2Db**). However, we did not observe such variability when we obtained multiple line scans across the same ribbon (**Fig. 2Da** vs. **Fig. 2Db,** gray traces). We wondered whether the observed variability between cells could be due to different rod BPCs in zebrafish [41], which might have different subtypes or numbers of Ca^{2+} channels near each ribbon. Immunolabeling of isolated BPCs preparation used in these experiments showed primarily intact BPCs which are PKC-α-specific RBC1-rod BPCs (**Supplementary Fig. 3B**). Moreover, these had special morphological characteristics; in particular, the shape and size of soma and single synaptic terminal [42]. Here, we refer to RBC1-rod BPCs as rod BPCs as they are similar to mammalian rod BPCs. Thus, we attribute the variability in the Ca^{2+} transients to the variability between the Ca^{2+} microdomains within the same cell type.

To further define Ca^{2+} signaling domains at the proximal and distal locations to the synaptic ribbon, we repeated the x-t line scan analysis with soluble lower affinity Ca^{2+} indicator Cal520LA (**Fig. 3**) in case the high-affinity indicator Cal520HA was saturated at the Ca^{2+} levels expected in these microdomains [43]. We found that the Ca^{2+} microdomains detected with Cal520LA (**Fig. 3**) exhibited depolarization-evoked Ca^{2+} (**Fig. 3Ab,** white arrowhead and **Fig. 3C,** black arrow) which was largely associated with the ribbon, as evident from the x-t raster plot (**Fig. 3Ab,** arrowhead vs. arrow), spatial profile (**Fig. 3B**, cyan trace), and temporal profile (**Fig. 3C**, red and blue traces vs. green trace). Furthermore, when compared to distal and cytoplasmic Ca^{2+} signals, the ribbon proximal signals showed a sharp rise and decay at the onset (**Fig. 3C,** black arrow) and termination of the stimulus, respectively, as expected for nanodomain Ca^{2+} signals [32-34]. The relationship between rise times (defined as time to half-maximal value) for the proximal (4.58 millisecond), distal (7.10 millisecond), and cytoplasmic Ca^{2+} (8.08 millisecond) signals were similar to those we found with Cal520HA, with the proximal and distal Ca^{2+} signals being faster than the cytoplasmic ones. In twenty-one similar experiments, the peak $\Delta F/F_{rest}$ at the membrane after 10-ms depolarization was significantly larger for proximal signals with 3.1 ± 0.4, 1.9 ± 0.2 for distal signals (P=0.001, N= 21, 95% confidence limit) and 1.4 ± 0.2 for cytoplasmic signals (P<0.001, N= 21, 95% confidence limit). The ratio between proximal to distal location measured with Cal520LA

(1.6) was substantially higher than that/those measured with Cal520HA (1.3), suggesting that the difference in kinetics/amplitude/etc., between proximal and distal Ca^{2+} signals is better defined with the low-affinity Ca^{2+} indicators.

Ribbon-bound Ca^{2+} indicators measure distinct local Ca^{2+} microdomains.

Next, we investigated whether the distinction between proximal and distal Ca^{2+} signals could be further refined using immobile Ca^{2+} indicators, as diffusible Ca^{2+} indicators report space-averaged Ca^{2+} concentrations, and their intracellular diffusion inherently broadens the spatial resolution of Ca^{2+} nanodomains. To partially? overcome this problem, we targeted the Ca^{2+} indicators to the ribbon by fusing them to the RBP, as described previously [20]. RBP-conjugated Ca^{2+} indicators Cal520HA-RBP or Cal520LA-RBP (Cal520-RBP) were introduced to the rod BPC terminal together with fluorescently labeled RBP via whole-cell voltage clamp by placing the patch pipette directly at the terminal while imaging the terminal using laser scanning confocal microscopy. For two-color imaging, ribbons were labeled with TAMRA-RBP that did not interfere with Cal520-RBP fluorescence, and both channels were scanned sequentially to prevent possible bleed-through. Under these conditions, we used the spots detected by TAMRA-RBP to define the locus of the synaptic ribbon (**Fig 4A&B, magenta**). In addition, we also found punctate regions in both Cal520HA-RBP (**Fig 4A, cyan**) and Cal520LA-RBP (**Fig 4B, cyan**) in the same location, on a background of a dimmer fluorescent terminal background, which are Ca^{2+} indicator-peptide complexes that are bound to and not bound to the ribbon respectively [20].

The overall changes in $\Delta F/F_{rest}$ were averaged over several trials for proximal and distal Ca^{2+} signals measured with Cal520HA-RBP (**Fig. 4C**, red vs. blue) and Cal520LA-RBP (**Fig. 4D,** red vs. blue). When compared to their distal location counterparts, the Ca^{2+} signals proximal to the membrane showed a sharper rise and decay at the onset and termination of stimuli, respectively (**Figs. 4C** and **4D**, red vs. blue trace) as expected for nano- and microdomain Ca^{2+} profiles. Our data shows that the amplitude of ribbon proximal and ribbon distal Ca^{2+} signals were well resolvable using the ribbon-bound Cal520HA-RBP indicator (**Fig. 4C**, red vs. blue traces; 3 ± 0.4 vs. 1.9 ± 0.3, respectively, $p<0.001$). However, ribbon-bound Ca^{2+} indicators with higher affinity were likely be saturated by local Ca^{2+} signals at the active zone within 500nm, and therefore local Ca^{2+} concentrations measured with Cal520LA-RBP are likely more accurate, and of higher values than those measured using higher-affinity indicators. Further, local Ca^{2+} concentration measurements achieved with bound indicators are likely to be higher than those reported by free indicators, as diffusion would rapidly shuttle

the Ca^{2+}-bound molecules of the free Ca^{2+} indicator away from the ribbon base. Indeed, the amplitudes of proximal and distal Ca^{2+} signals were higher when measured with Cal520LA-RBP than Cal520LA-free (proximal, **Fig. 4E**, red (bound) vs. pink (free); 5.5 ± 0.9, n=30 vs. 3.1 ± 0.4, n=21, p=0.04 and distal, **Fig. 4F**, dark (bound) vs. light blue (free); 3.3 ± 0.8, n=30 vs. 1.9 ± 0.2, n=21, p=0.15). Together, these findings strongly suggest that conjugating the Cal520LA indicator to RBP so that it is bound to the ribbon rather than diffusing away the ribbon provided a better approach for measuring the distinct local Ca^{2+} signals at ribbon-proximal vs. ribbon-distal locations with our recording conditions used in these experiments.

Ca^{2+} concentrations at single ribbon locations during depolarization.

To estimate the Ca^{2+} concentration gradient along the ribbon, we obtained the ratiometric measurements with RBP-conjugated Ca^{2+} indicator and normalized to those of RBP-peptides conjugated to Ca^{2+}-insensitive fluorophores (TAMRA-RBP). We obtained the effective $K_{1/2}$(K_{eff}) by measuring the fluorescence of the Cal520HA-RBP/ TAMRA-RBP ratio in buffered Ca^{2+} solutions and using the Grynkiewicz equation [44]. We found the K_{eff} of for Cal520HA-RBP to be ~795 nM, which is higher than the value of 320 nM reported by the manufacturer for Cal520HA. The differences between the in-cell measurements and the manufacturer's values are likely to arise from differences in the cellular buffering capabilities, changes in dye properties due to interacting with molecules inside the cell [45-48], and possible differences in the binding properties of the peptide-conjugated Ca^{2+} indicators when bound to synaptic ribbons. Since the in-cell approach most closely matched the experimental conditions, we used this value (K_{eff}) for all further calculations.

We first measured the proximal to distal Ca^{2+} concentration gradients on the ribbon using Cal520HA-RBP with 0.2 mM EGTA in the patch pipette as it allowed us to distinguish the gradients between the two (**Fig. 4A)**. Under these conditions, we found a maximum proximal Ca^{2+} concentration of 3.7 μM, and a maximum distal Ca^{2+} concentration of 0.7 μM. These Ca^{2+} concentration measurements with Cal520HA-RBP likely represent the lowest Ca^{2+} concentration at a single ribbon location in response to a brief 10-ms pulse. However, the measured Ca^{2+} concentration at the ribbon location with Cal520HA-RBP was well below the amount required to trigger UFRP and RRP [43], as discussed earlier, due to local saturation of the high-affinity indicator and/or to nanodomains that are smaller than the resolution attainable using light microscopy. It should

be noted that unlike freely diffusing Ca^{2+} indicators, RBP-conjugated indicators that slowly unbind from the ribbon are not readily replaced by free Ca^{2+} indicators, rendering them more prone to saturation. Therefore, the quoted values should be viewed as lower bounds on the proximal [Ca^{2+}] value. Nevertheless, our data demonstrate that ribbon-bound indicators can better report local Ca^{2+} concentrations due to their localization, albeit still subject to the limitations of light microscopy.

To test the contribution of local saturation and to better estimate ribbon Ca^{2+} concentrations, we repeated our measurements using the low-affinity Ca^{2+} indicator Cal520LA conjugated to the RBP peptide. Because it was difficult to perform in-cell measurements to determine the K_{eff} for Cal 520LA-RBP given the large amounts of Ca^{2+} required to calibrate the Cal 520LA indicator (Methods and Materials), we used the pipette measurements for Cal520LA-RBP as K_{eff} (90 μM), which were similar to the $K_{1/2}$ *value* provided by the manufacturer for free Cal520LA (90 μM). However, we expect that in-cell measurement of $K_{eff,}$ are likely to be different due to the cellular buffering properties reported previously for $K_{eff,}$ measurements of Oregon Green BAPTA-5N in inner hair cells [45].

Significant evidence from several groups indicates that BPCs can also release neurotransmitters via non-ribbon (referred as NR) mechanisms [49-51]. The source of Ca^{2+} for this release could be Ca^{2+} channels outside the ribbon sites or Ca^{2+} that diffuses away from channels that are clustered at ribbon sites. To reveal the Ca^{2+} signaling at and away from the ribbon, we performed whole-cell patch clamping and x-t line scans at ribbon (**Fig. 5Ba**, ribbon) and non-ribbon (**Fig. 5Bb,** NR) sites perpendicular to the plasma membrane using TAMRA-RBP and Cal520LA-RBP. **Fig.5B** shows the raster plots of Cal520LA-RBP/TAMRA-RBP fluorescence as a function of time obtained at ribbon (**Fig. 5Ba,** ribbon) and non-ribbon near-membrane locations (**Fig. 5Bb,** NR). A brief (10-ms) depolarizing voltage-clamp pulse evoked rapid high Ca^{2+} signals (**Fig. 5Ba**, green raster plot) at ribbon locations (**Fig. 5Ba,** red raster plot**)** but not at non-ribbon locations (**Fig. 5Bb**, green raster plot). The amplitude of Ca^{2+} signals elicited by brief depolarization and detected with Cal520LA-RBP at the ribbon-proximal site (**Fig. 5C**, red traces) were significantly higher than those at ribbon distal (**Fig. 5C**, blue traces), and non-ribbon (**Fig. 5C**, purple traces) sites. The Ca^{2+} concentration gradient along the ribbon is summarized in **Fig. 5D d**espite substantial variability of local Ca^{2+} signals between cells, we found that the average Ca^{2+} concentration at the proximal side of the ribbon (26.4 ± 3.1 μM, n=26) was significantly different from that at the distal (15.6 ± 1.5 μM, n=26) and non-ribbon (10.4 ± 0.4 μM, n=15) sites, with that at distal sites being higher

than those at non-ribbon sites (**Fig. 5C**). These measurements display large heterogeneity across distinct ribbons and distinct cells, with the coefficient of variation of about 60% for [Ca^{2+}] measurements at locations proximal to the ribbon, compared to a 10% CV for multiple depolarizations for the same ribbon. The Ca^{2+} signals at distal sites also reached their peak amplitude earlier (**Fig. 5C *inset***, blue arrowhead) than those at the non-ribbon sites (**Fig. 5C *inset***, purple arrowhead). These findings are consistent with non-ribbon vesicle release being governed by cytoplasmic residual Ca^{2+} or Ca^{2+} influx via clustered Ca^{2+} channels at ribbon sites rather than non-ribbon active zones with clusters of Ca^{2+} channels and with previous reports regarding their sensitivity to EGTA and the temporal delay in non-ribbon release [50,52].

Computational models of local Ca^{2+} signals.

Resolving Ca^{2+} signals associated with the Ca^{2+} domain that controls ultrafast releasable pool (UFRP) release is currently impossible due to the finite spatiotemporal resolution of optical imaging. In particular, spatial diffusion, dye saturation, and dye binding kinetics all smooth out the peak of the Ca^{2+} transients in the nanodomain near Ca^{2+} channels. To better understand the features of Ca^{2+} signals in these critical locations, we tried to fit our data and placed limits on the underlying properties of Ca^{2+} signals at the base of the ribbon. Since we could identify the position of the ribbon and used fused Ca^{2+} indicator-RBP, we were able to measure and distinguish proximal vs. distal Ca^{2+} signals that drive the release of UFRP and RRP. However, several factors, including finite spatiotemporal resolution of optical imaging, spatial diffusion, dye saturation, and dye binding kinetics, may limit our ability to achieve optimal resolution. These limitations, however, may be overcome by the use of quantitative models. Thus, we developed a model based on our data with published information for Ca^{2+} diffusion and buffering to estimate the estimated ranges of the Ca^{2+} current per ribbon and $[Ca^{2+}]_i$ gradient along the ribbon at distinct distances from the plasma membrane. **Fig. 6** describes the geometry of the model simulation that we used to estimate spatiotemporal [Ca^{2+}] dynamics near the synaptic ribbon, with the simulation results shown in **Fig. 7**.

Combining whole-terminal Ca^{2+} current measurements and our estimate for the number of synaptic ribbons per terminal allows us to infer the magnitude of Ca^{2+} current per single ribbon (**Supplementary Fig. 5**), which we use to model the spatiotemporal [Ca^{2+}] dynamics near the ribbon. **Fig. 7** shows the results of the simulation of [Ca^{2+}] at various distances from the ribbon during and after a depolarizing pulse of 10ms used in

our experiments in the presence of different concentrations of exogenous and endogenous buffers. The geometry of the simulation domain box is shown in **Fig. 6**; it represents the fraction of total synaptic terminal volume per single ribbon (see Methods, **Table 1** and **Supplementary Fig.5**.). **Fig. 7** shows the time-dependence of [Ca^{2+}] during and after the depolarization pulse at 5 specific locations both near and far from the ribbon (left-hand panels in each subplot). These five spatial locations are marked by circles of different colors in the right-hand panel of each subplot, which shows [Ca^{2+}] in pseudo-color in the entire planar cross-section of the simulation domain cutting through the middle of the ribbon, as shown in **Fig. 6**, right at the end of the Ca^{2+} current pulse. We assumed a highly simplified Ca^{2+} channel arrangement into four clusters forming a square with a side length of 80nm. The closest location (red curves and circles in **Fig. 7**) is X=20 nm away from the base of the ribbon center-line, Z=10 nm above the ribbon, about 45nm away from the closest Ca^{2+} channel cluster (see **Fig. 6**). We assumed that this location was within the Ca^{2+} microdomain that triggered the release of the UFRP. Vesicles were not included in the simulation since the total exclusion volume attributed to them represented only a small fraction of the total inter-terminal volume and, therefore, did not significantly impact [Ca^{2+}] at the qualitative resolution level we were interested in. A couple of simulations with vesicles included were performed to confirm this statement, requiring much finer spatial resolution and larger computational time. We note also that [Ca^{2+}] for short pulse durations considered here is relatively insensitive to our assumptions on the membrane Ca^{2+} extrusion mechanisms, listed in **Table 1.**

Fig. 7A1-B2 reveals that [Ca^{2+}] could rise above 50 μM within the microdomain near the base of the ribbon in the presence of 0.2 mM up to 10 mM EGTA. Given the size of the microscope point-spread function, this is in qualitative agreement with the 26 μM estimate of proximal [Ca^{2+}] that we recorded using the ribeye-bound low-affinity indicator. In addition, this is the concentration level reached very soon after the channel opening event due to the rapid formation of the Ca^{2+} microdomain [53,54], and therefore this estimate is expected to hold for shorter pulses as well. However, [Ca^{2+}] decayed rapidly with distance, with the rate of decay significantly increasing when EGTA concentration was increased to 10mM (**Fig. 7B1, B2**). Note that a 7-fold change in the capacity of the immobile endogenous Ca^{2+} buffer (cf. **Fig. 7A1 vs. 7A2**) had a relatively modest effect on the [Ca^{2+}] level up to about 150 nm distance from the ribbon base. This effect of increasing endogenous buffer concentration was further reduced in 10 mM EGTA (cf. **Fig. 7B1 vs. 7B2**), due to strong competition of large concentrations of EGTA with the endogenous buffer. This agrees with the expectation that

immobile buffers primarily slow down Ca^{2+} signals but do not affect the rapidly forming quasi-steady-state Ca^{2+} microdomains in the immediate vicinity of the channel [53-55]. Finally, **Fig. 7D1-D2** shows that 2 mM BAPTA had a much greater effect on localizing the Ca^{2+} signal to the immediate vicinity of the ribbon base.

Since a native unpatched cell may well contain mobile rather than immobile buffers, it was interesting to examine the effect of increasing the concentration of mobile endogenous buffer on Ca^{2+} dynamics in the ribbon vicinity, as compared to the corresponding effect of immobile buffer. **Supplemental Figure 4** shows that a 7-fold increase in mobile buffer concentration reduces the microdomain Ca^{2+} by a factor of 2, and greatly reduces the size of the microdomain. This contrasts with the effect of increasing the concentration of the immobile buffer, which has a much more subtle effect (cf. **Fig. 7A1, A2**). We note that 0.2 mM EGTA was absent in the simulation with mobile buffer shown in **Supplemental Figure 4**; in general, the effect of modest concentrations of EGTA is expected to be negligible due to its slow Ca^{2+} binding speed compared to the immobile buffer.

Ca^{2+} gradient at different locations along the synaptic ribbon.

Previous work has shown that the rate of vesicle replacement in rod BPCs is accelerated by elevated Ca^{2+} levels at sites along the ribbon and that while millimolar levels of EGTA have little effect on the fast exocytosis component near Ca^{2+} channels, they selectively block the sustained exocytosis, likely by preventing Ca^{2+} from reaching the distal locations on the ribbon [11,56-59]. These findings raise the possibility that Ca^{2+} has two sites of action, one near the Ca^{2+} channels that triggers vesicle release and one further away that replenishes the supply of releasable vesicles. Burrone *et al.* (2002) proposed that endogenous Ca^{2+} buffers regulate the size of the RRP by limiting the spatial spread of Ca^{2+} ions, thereby suppressing vesicle release at the periphery of the active zone in BPCs [7]. However, the Ca^{2+} gradient at different locations along the ribbon controlling RRP release has never been examined.

Thus, we used our nanophysiology approach (**Fig.1**) to measure the Ca^{2+} gradient along the synaptic ribbon under buffering conditions that differentially modulate proximal vs. distal Ca^{2+} pools and to examine whether heterogeneity in Ca^{2+} signals could be due to differences in local Ca^{2+} buffering. To determine the spatiotemporal properties of Ca^{2+} signals under these conditions, we performed rapid x-t line scans at a single ribbon location in the presence of Cal520HA-RBP and varying concentrations of exogenous buffer in the patch

pipette solution, including EGTA at 0.2 (**Fig. 8A**), 2 (**Fig. 8B**), and 10 mM (**Fig. 8C**) or BAPTA at 2 mM (**Fig. 8D**). We found that the ratio between proximal and distal Ca^{2+} signals was similar in 0.2 and 2 mM EGTA (proximal-to-distal ratio ~1.5, **Supplementary Table 2**), but was enhanced with 10 mM EGTA (proximal-to-distal ratio ~2.6, **Supplementary Table 2**) and further enhanced with 2 mM BAPTA (proximal-to-distal ratio ~2.8, **Supplementary Table 2**). The temporal and spatial profiles of Cal520HA-RBP show that cytoplasmic Ca^{2+} concentrations were substantially lowered under these conditions, and in the presence of 2 mM BAPTA, the cytoplasmic Ca^{2+} signals were completely abolished (**Fig. 8D**) with the remainder of the Ca^{2+} signals largely restricted to the location proximal to the ribbon where the Ca^{2+} channels reside (**Fig. 8Dc**, white arrowhead). Previous studies in goldfish suggested that the UFRP pool (**Supplementary Fig. 2,** green vesicle) would be impervious to 5 mM EGTA, but not to 5 mM BAPTA [11]. However, in mouse rod BPCs, exocytosis is largely insensitive to the exogenous Ca^{2+} chelators, particularly to 1.5 mM BAPTA [12]. These findings suggest that high buffering can restrict the Ca^{2+} signal spread but have minimal effect on the UFRP. However, at some point, high BAPTA should restrict it so much that it can block release, as shown in Mennerick and Matthews's studies in goldfish [11]. Our capacitance measurements with varying concentrations of exogenous buffer findings aligned with Singer and Diamond's studies [12]. The average capacitance measurements for 0.2 EGTA, 2 EGTA, 10 EGTA and 2 mM BAPTA, were 21.3 $\pm$ 2 fF (n=24), 23.8 $\pm$ 1.8 fF (n=21), 22.6 $\pm$ 2.9 fF (n=31) and 21 $\pm$ 1.9 fF (n=20), respectively. Further, we observed no changes in vesicle release efficiency in 2 mM EGTA, 10 mM EGTA, or 2 mM BAPTA relative to 0.2 mM EGTA (**Supplementary Fig. 6**). We thus infer that calcium signals in response to 10 ms stimuli obtained with our recording conditions largely control docked UFRP release. Indeed, if single vesicle capacitance is 26.4 aF, 21 fF in 2 mM BAPTA is about 795 vesicles, and if we have 40 ribbons, is about 21vesicles/ribbon), which is likely to be all docked vesicles as shown previously in goldfish bipolar cells [60]. Further, we observed no changes in vesicle release efficiency in 2 mM EGTA, 10 mM EGTA, or 2 mM BAPTA relative to 0.2 mM EGTA (**Supplementary Fig. 6**)**,** suggesting a tight coupling between calcium channels and influx.

Cal520 acts as a buffer that binds Ca^{2+} and diffuses away with it. The higher affinity indicator Cal520HA will bind and shuttle away more Ca^{2+} than Cal520LA. If the Cal520HA indicator is saturated near the Ca^{2+} channels, it may be missing the fast Ca^{2+} transients that occur in those locations. Thus, we also measured the spatiotemporal properties of local Ca^{2+} signals using ribbon-bound Cal520LA-RBP with varying concentrations

of exogenous buffer (**Supplementary Fig. 7**) as above for Cal520HA-RBP (**Fig. 8**). We found that the ratio between proximal and distal Ca^{2+} signals was similar in 0.2 and 2 mM EGTA (proximal-to-distal ratio ~1.7, **Supplementary Table 3**) but was enhanced with 10 mM EGTA (proximal-to-distal ratio ~1.9, **Supplementary Table 3**) and further enhanced with 2 mM BAPTA (proximal-to-distal ratio ~4.5, **Supplementary Table 3**). These experimental findings of increasing ratio of proximal-to-distal Ca^{2+} signal with increasing EGTA concentration indeed are in agreement with the simulation results, although given the large size of the point-spread function, the corresponding ratios are greater in the simulation than in the experiment. Capacitance measurements and vesicle release efficiency in experiments using Cal520LA-RBP and varying concentrations of exogenous buffer showed no difference (data not shown), confirming that the nanodomain of high Ca^{2+} signals controls UFRP release.

Though BAPTA significantly abolished the spread of Ca^{2+} signals, it is impressive that a substantial amount of proximal Ca^{2+} signals was still present with 2 mM BAPTA. One reason for the observed proximal Ca^{2+} signals with 2 mM BAPTA could be that ribbon-bound Ca^{2+} indicators are likely to measure Ca^{2+} signals very close to Ca^{2+} channels without diffusing away and that BAPTA is not able to block the Ca^{2+} signals closer to the Ca^{2+} channels. If so, similar experiments conducted with free Ca^{2+} indicators should report a significantly lower apparent proximal Ca^{2+} signal since the measurement by a diffusible dye would effectively spread out the signal over a larger volume. Indeed, this is what we found. As shown in **Supplementary Fig. 8,** the apparent proximal Ca^{2+} signal in response to a 10-ms brief pulse with 2 mM BAPTA measured with Cal520LA-free was 0.8 ± 0.2 (n=9), 4.5-fold lower than proximal Ca^{2+} signals measured with Cal520LA-RBP (3.6 ± 1, n=20). The latter value is closer to the true measure of the Ca^{2+} concentration in the vicinity of the ribbon base. These findings once again emphasize the much needed spatial resolution of our approach to measuring reliable ribbon proximal Ca^{2+} signals, where Ca^{2+} channels are located.

Variability of local Ca^{2+} signals in the rod bipolar cell terminal.

BPCs release neurotransmitters primarily from ribbon active zones, although some release also occurs at non-ribbon sites [49-51]. However, the factors that shape the synaptic ribbon microdomains in retinal ribbon synapses have not been examined. We wondered whether all of the 30~50 synaptic ribbons release glutamate in a similar fashion or whether there is some heterogeneity in glutamate release from different ribbon active zones.

In particular, we asked what underlying mechanisms could differentiate the Ca^{2+} signals between ribbons of the same or different rod BPCs.

To identify the mechanisms that contribute to the heterogeneity in the local Ca^{2+} signals we have reported in this study, we began by asking whether differences in local Ca^{2+} buffering could account for this heterogeneity. To examine the role of Ca^{2+} buffering in the variability of local Ca^{2+} signals across different cells and different ribbons (**Figs. 2D, 9A** and **9B)**, we compared proximal (**Figs. 9B** and **9E**) and distal (**Figs. 9C** and **9F**) Ca^{2+} signals in 10 mM EGTA by averaging the Ca^{2+} recordings from all the ribbons of a given cell (**Supplementary Figs. 9** and **10**) using R Studio software (Version 2023.09.0+463). When the Ca^{2+} signals were restricted to the ribbon sites with 10 mM EGTA in the pipette solution (**Supplementary Tables 2** and **3**), the amplitude of the local proximal and distal Ca^{2+} signals averaged over all ribbons of a given cell exhibited significant variation across different cells (**Figs. 9B, 9C,** and **Supplementary Fig. 9**). We next compared variability in Ca^{2+} signals in the presence of 10 mM EGTA at individual ribbons *within the same cell* (**Fig. 9D** and **Supplementary Fig. 10**) at proximal (**Fig. 9E**) and distal (**Fig. 9F**) locations. For the cell described in **Figs. 9E-9F**, the proximal Ca^{2+} signals were significantly different across all ribbons examined, and there were considerable differences in distal Ca^{2+} signals between all distinct ribbons, with the exception of ribbons 2 and 5. These findings suggest that the heterogeneity in proximal and distal Ca^{2+} signals at distinct ribbons within the same cell may result from different underlying mechanisms. In addition, our analysis also indicates that variability in ribbon-averaged proximal Ca^{2+} signals was also preserved after addition of 2mM BAPTA in individual ribbons between cells and within the same cells (data not shown), suggesting that exogenous Ca^{2+} buffering has a negligible effect on experimentally observed heterogeneity and variability of the proximal Ca^{2+} signals in some ribbon active zones and that local Ca^{2+} signals in these ribbons are dominated by Ca^{2+} in regions close to the ribbon base where Ca^{2+} channels are located.

The ultrastructure of the zebrafish bipolar cell terminal reveals diversity in the size of the synaptic ribbon.

In hair cells, Ca^{2+} microdomain signaling varied with ribbon size, reflecting larger patches of Ca^{2+} channels aligned with larger ribbons [23]. We next sought to determine whether similar heterogeneities in ribbon size existed in the fish RBPs. The first observed evidence for such variability was in our confocal images of

fluorescently labeled RBP and Ca^{2+} indicators conjugated to RBP, which showed variability in ribbon size and Ca^{2+} hot spots (data not shown) as shown previously in hair cells [23]. However, the resolution of our confocal images is insufficient to distinguish two ribbons that are close together in a cell. To provide quantitative measurement of ribbon microdomains, we obtained the ultrastructure of retinal rod bipolar cells using serial block-face scanning electron microscopy (SBF-SEM). We analyzed the BPCs that are closest to the ganglion cells that are similar to those previously referred to as RBC1 and resemble mammalian rod BPCs (**Fig. 10D**) [41].

Here, we report for the first time significant variations in the shape and size of synaptic ribbons in rod BPCs (**Fig. 10**). On average, individual ribbons spanned 2–5 consecutive sections, with some located within the axons, closer to the terminal. We observed a similar pattern of ribbons in the axons of living bipolar cell neurons voltage-clamped with the patch-pipette solution containing fluorescently labeled RBP by confocal microscopy (data not shown). The EM images and 3D projections of ribbon structures (colored in magenta) revealed considerable variability in shape and size across all dimensions, as illustrated in **Figs. 10A–10C.**

We wondered whether variation in the ribbon morphology could be correlated to variation in the number of Ca^{2+} channels tethered to the synaptic ribbons. The number of Ca^{2+} channels per active zone in hair cells from chicken, frog, and turtle vary with the size of the synaptic ribbon [61]. Therefore, we measured the area of the ribbon facing the plasma membrane where the Ca^{2+} channels are known to be located to estimate the number of Ca^{2+} channels per active zone. The EM images and 3D projection of the plasma membrane (yellow) and the area of the ribbon facing the plasma membrane (cyan) are shown in **Figs. 10A-10C**. We observed large variability in the area of the ribbon facing the plasma membrane within the BPCs, with substantial variability in the average distribution of three rod BPCs (**Figs. 10C, cyan** and **10E** and **Supplementary Fig. 10A)**, suggesting that the number of Ca^{2+} channels per active zone are also likely varied. **Supplementary Fig. 10B** shows a reconstruction of three rod bipolar cells with 30~41 ribbons, which is similar to what was previously reported in goldfish Mb1 BPCs (ranging from 45~60 [60]).

Discussion

A deep look at the active zone Ca^{2+} microdomain in rod bipolar cells. In this study, we use fast spatially resolved imaging of ribbon-attached and soluble fluorescent Ca^{2+} indicators to measure Ca^{2+} dynamics in zebrafish retinal rod BPCs. We studied the local Ca^{2+} signals that control kinetically distinct neurotransmitter

release components at a single ribbon active zone using Ca^{2+} indicators with different affinities and rapid x-t line-scans and identified spatially confined Ca^{2+} domains in areas of the synaptic ribbon proximal to the membrane that exhibited higher levels of Ca^{2+}.

We showed previously the selective fusion of membrane-proximal synaptic vesicles during brief depolarization pulses and estimated that the Ca^{2+}concentration near the membrane likely exceeds 10μM within 3 milliseconds after the opening of the Ca^{2+} channels with rapid x-t line-scans at a single ribbon active zone using soluble Ca^{2+} indicators [19]. In the current study, we established a quantitative nanophysiology approach using ribeye-bound Ca^{2+} indicators and fluorescently labeled RBP, conducting ratiometric dual color imaging to measure the changes in the Ca^{2+} concentration at and along the axis of the ribbon. Using Ca^{2+} indicators targeted to the ribbon together with fluorescently labeled RBP to increase the spatial resolution of the Ca^{2+} nanodomains, we determined that the Ca^{2+} concentration near the membrane could increase to an average of 26 μM on depolarization. These measurements are closer to the $[Ca^{2+}]_i$ levels required for the activation of rapid, transient component of exocytosis, in agreement with previous results suggested for rod BPCs [14,43,62]**.** Previous work on rod BPCs found slowing of recovery from paired-pulse depression by EGTA, suggesting Ca^{2+} levels at distal sites on the ribbon might be important for the recruitment of new vesicles following depletion of the RRP and UFRP [11,37]. Here, we measured directly the effect of EGTA on the spread of Ca^{2+} signals and found that the Ca^{2+} signal at the distal half of the ribbon was two-fold lower than that proximal to the membrane under conditions of low Ca^{2+} buffering. These findings suggest that despite the technical challenges posed by the limited spatiotemporal resolution of optical imaging, the spatial resolution attained with the nanophysiology approach developed in our study is sufficient to differentiate Ca^{2+} signals associated with distal sites on the ribbon from those localized near the plasma-membrane. It should be noted, however,that diffraction of light during the optical imaging procedure likely to underestimate spatiotemporal $[Ca^{2+}]$ along the ribbon. Therefore, we used our measurement of the per ribbon Ca^{2+} current to develop a detailed computational model that allowed us to resolve the expected profile of the Ca^{2+} microdomains governing UFRP fusion. The model results shown in **Fig. 7** reveal on a finer spatial scale the distribution of Ca^{2+} around a ribbon in the presence of various quantities of immobile endogenous buffer and added exogenous buffers. Our finding of high proximal $[Ca^{2+}]$ levels on the order of 26 μM recorded using a ribeye-bound low-affinity indicator dye is in qualitative agreement with the simulated high concentration of Ca^{2+} in the microdomain at the base of the ribbon.

Simulations also show that, as expected, the microdomain Ca^{2+} amplitude is relatively insensitive to the concentration of endogenous immobile buffer and added EGTA, but its decay with distance is accelerated by increasing the concentrations of exogenous and endogenous buffers. In contrast, addition of 2 mM BAPTA causes a profound reduction of the Ca^{2+} microdomain amplitude and localizes the signal to a small volume around the ribbon. We also compared the impact of mobile vs immobile endogenous buffers on the Ca^{2+} distribution, showing the much greater effect of mobile buffer on the microdomain amplitude and distance dependence. Although these results are generally expected[53-55], the simulation results estimate the [Ca^{2+}] levels in the vicinity of the ribbon with greater spatial and temporal resolution. As expected, the ratios of Ca^{2+} concentration values at the base of the ribbon vs. further away from the ribbon are much greater in the simulation than our experimentally determined proximal-to-distal Ca^{2+} ratio values, due to the large size of the microscope PSF precluding precise localization of the corresponding Ca^{2+} signals. Further, simulations show the effect of exogenous buffers with greater spatial resolution. However, the simulations fully agree with the overall increasing trend of the proximal-to-distal Ca^{2+} concentration ratios by the application of exogenous Ca^{2+} buffers, and especially BAPTA. Conceivably, our nanophysiology approaches established here should generally apply to other classes of bipolar cells and other sensory ribbon synapses for measuring individual ribbon Ca^{2+} signals.

Heterogeneity of Ca^{2+} microdomains in bipolar cells. Our quantitative nanophysiology approach suggests heterogeneity in the Ca^{2+} microdomain and in the size of ribbons between and within retinal BPC at distinct ribbon active zones. Retinal bipolar neurons contain many ribbon active zones ranging from 45~60 in adult goldfish, as quantified by EM [60], 25~45 in bipolar cells of adult living zebrafish as estimated from laser scanning confocal microscopy images of fluorescently labeled RBP and counting the resulting deconvoluted images with Imaris software [63], or approximately 31~40 in zebrafish bipolar cells as visualized in this study by SBF-SEM. The higher variability in the number of ribbons found in confocal compared to SBF-SEM images may be explained by PSF limitation in confocal images. Previous studies in cone photoreceptors found that Ca^{2+} signal amplitude and midpoint activation voltage at individual ribbons varied among ribbons within cones. Further, they also reported that local Ca^{2+} signal changes at ribbons can be regulated independently [21]. Heterogeneity between ribbon active zones has been previously reported in hair cells where synaptic Ca^{2+}

microdomains varied substantially in amplitude and voltage-dependence within individual inner hair cells [22,23]. These heterogeneities likely contribute to the variability of spontaneous and evoked rates, sound threshold, and dynamic range among spiral ganglion neurons of similar characteristic frequency.

Our findings add further complexity to the diversity of the bipolar cells' output to amacrine cells and ganglion cells. Future studies uncover the distinct mechanisms related to the heterogeneity observed in the distal Ca^{2+} signals, such as revealing differences in Ca^{2+} release from intracellular stores or Ca^{2+} sequestration [64]. Although the potential impact of these sources on Ca^{2+} microdomain heterogeneity in hair cells has not been reported,[23] previous studies in goldfish BPC terminals have documented spatially restricted Ca^{2+} oscillations in voltage-clamped retinal BPCs, occurring independently of membrane potential. [20] To our knowledge, the sources of Ca^{2+} for these oscillations remain unknown. However, previous studies in goldfish bipolar cells suggest that the endoplasmic reticulum[64] and mitochondria[18] may act as internal calcium stores. Notably, IP_3 receptors have been localized to retinal BPC terminals in some species.[65,66] The heterogeneity in rod BPCs reported in this study may contribute to the dynamic range of rod bipolar cell ribbon synapses[25-27]—a hypothesis to be tested in future studies, as discussed previously for hair cells and cone ribbon synapses [21-23,28,29].

Methods

Rearing of zebrafish. Male and female zebrafish (*Danio rerio*; 16 ~20 months) were raised under a 14 h light/10 h dark cycle and housed according to NIH guidelines and the University of Tennessee Health Science Center (UTHSC) Guidelines for Animals in Research. All procedures were approved by the UTHSC Institutional Animal Care and Use Committee (IACUC; protocol # 23-0459).

Isolation of zebrafish retinal rod bipolar cells. Dissociation of rod BPCs was performed using established procedures [67]. Briefly, retinas were dissected from zebrafish eyes and incubated in hyaluronidase (1100 units/ml) for 20 minutes. The tissue was washed with a saline solution containing 120 mM NaCl, 2.5 mM KCl, 0.5 mM $CaCl_2$, 1 mM $MgCl_2$, 10 mM glucose, and 10 mM HEPES, pH = 7.4] before being cut into quadrants. Each quadrant was incubated at room temperature for 25 to 40 min in the same saline solution, to which was added DL-cysteine and papain (20-30 units/ml; Sigma Millipore, St. Louis, MO) and triturated using a fire-

polished glass Pasteur pipette. Individual cells were transferred to glass-bottomed dishes, allowed to attach for 30 minutes, and washed with saline solution before being used for experiments.

Ribeye binding peptides. As a means of localizing the ribbons, custom peptides containing the ribbon binding sequence fused to TAMRA (tetramethylrhodamine; TAMRA: GIDEEKPVDLTAGRRAG) dye were synthesized, purified, and purchased from LifeTein (>95% purity, LifeTein LLC, NJ).

Ca^{2+} indicators.

*Free Ca^{2+} indicators***.** The potassium salts of high and low-affinity Ca^{2+} indicators Cal-520® (high affinity, K_D 320 nM) and Cal-520N™ AM (low affinity, K_D 90 μM), referred to as Cal520HA and Cal520LA, respectively were purchased from AAT Bioquest.

Direct conjugation of Ca^{2+} indicator to cysteine-containing ribbon-binding peptides. To target Ca^{2+} indicators to the ribbon, custom-made cysteine-containing ribeye binding peptides NH_2-CIEDEEKPVDLTAGRRAC-COOH were synthesized and purchased from LifeTein to directly fuse with the fluorogenic 520® maleimide (purchased from AAT Bioquest) for high affinity (HA) and low affinity (LA Ca^{2+} indicator dyes). Each peptide at 1 mM concentration was mixed and incubated with 2 mM Cal-520® maleimide (20 mM stock solution in DMSO purchased from AAT Bioquest) for 1 h, at room temperature then overnight at 4°C. Calibration of Ca^{2+} indicator dyes was performed as described [19] and as detailed below. The conjugated Ca^{2+} indicators were stored at -20°C in smaller aliquots, each sufficient for a single day's experiments.

Measurement of dissociation constants (K_D) for Ca^{2+} indicator peptides. The effective K_D (K_{eff}) was obtained by measuring the fluorescence of Cal520HA-RBP and TAMRA-RBP in buffered Ca^{2+} solutions, determining the ratio between them [19] , and using the Grynkiewicz equation to determine the Ca^{2+} concentration [Ca^{2+}] from this ratio [44]. However, this was not possible for the low-affinity indicator Cal520LA due to the large Ca^{2+} levels required to calibrate it. Thus, K_{eff} for Cal520LA-RBP could be larger than the $K_{1/2}$ provided by the manufacturer for Cal520LA (K_D, 90 μM), as reported previously with $K_{eff,}$ measurements of OB-5N in inner hair cells [45]. Thus, our estimates of local Ca^{2+} concentrations obtained using Cal520LA

represent the lower bounds of the underlying true values. As noted in the Results section, the same may be true for the high-affinity Cal520HA despite its accurate K_{eff} estimate, due to potential dye saturation effects.

Rod bipolar cell voltage clamp recording. Whole-cell patch-clamp recordings were made from isolated BPCs, as described previously [19,68,69]. Briefly, a patch pipette containing pipette solution (120 mM Cs-gluconate, 10 mM tetraethyl-ammonium-Cl, 3 mM $MgCl_2$, 0.2 mM *N*-methyl-d-glucamine-EGTA, 2 mM Na_2ATP, 0.5 mM Na_2GTP, 20 mM HEPES, pH = 7.4) was placed on the synaptic terminal, as described previously. The patch pipette solution also contained a fluorescently-labeled RBP peptide (TAMRA-RBP) to mark the positions of the ribbons and either 1) free Ca^{2+} indicators Cal520HA-free (**Figs. 1 and 2**) and Cal520LA-free (**Fig. 3**) to demonstrate our nanophysiological approach or 2) ribeye-bound Ca^{2+} indicators Cal520HA-RBP (**Figs. 4, and 8**) and Cal520LA-RBP (**Figs. 4, 5, 9, and Supplementary Figs. 7 and 8**) to measure local ribbon-associated Ca^{2+} signals. Current responses from the cell membrane were recorded under a voltage clamp with a holding potential (V_H) of -65 mV that was stepped to 0 mV (t_0) for 10 milliseconds. These responses were recorded with a patch clamp amplifier running PatchMaster software (version v2x90.4; HEKA Instruments, Inc., Holliston, MA). Membrane capacitance, series conductance, and membrane conductance were measured via the sine DC lock-in extension in PatchMaster and a 1600 Hz sinusoidal stimulus with a peak-to-peak amplitude of 10 mV centered on the holding potential [70].

Acquisition of confocal images. Confocal images were acquired using an Olympus model IX 83 motorized inverted FV3000RS laser-scanning confocal microscopy system (Olympus, Shinjuku, Tokyo, Japan) running FluoView FV31S-SW software (Version 2.3.1.163; Olympus, Center Valley, PA) equipped with a 60 X silicon objective (NA 1.3), all diode laser combiner with five laser lines (405, 488, 515, 561 & 640 nm), a true spectral detection system, a hybrid galvanometer, and a resonant scanning unit. Rapid x-t line scans of the zoomed region of a selected ribbon, centered around red fluorescent RBP signal were acquired to monitor fluorescence of the Ca^{2+} indicator dye (green). The focal plane of the TAMRA-RBP signal was carefully adjusted for sharp focus to avoid potential errors arising from the high curvature near the top of the terminal and the plane of membrane adherence to the glass coverslip at the bottom of the terminal. Acquisition parameters, such as pinhole diameter, laser power, PMT gain, scan speed, optical zoom, offset, and step size were kept constant

between experiments. Sequential line scans were acquired at 1-2 millisecond/line and 10 μs/pixel with a scan size of 256 × 256 pixels. The image acquisition time was confirmed via transistor-transistor logic (TTL) pulses between the FluoView and PatchMaster software used for patch-clamping (HEKA) in parallel with acquisition of voltage-clamp data.

Bleed-through between the channels was confirmed with both lasers using the imaging parameters we typically use for experiments in bipolar cells isolated from wild-type (WT) zebrafish. To test bleed-through from the RBP channel (TAMRA-RBP) to the Ca^{2+} indicator (Cal-520HA and Cal-520LA), whole-cell recordings from BPCs terminal were performed with patch pipette solution that contained TAMRA-RBP or the aforementioned Ca^{2+} indicators, and line-scan images were collected and analyzed using the same procedures used for experimental samples.

Point spread function. The lateral and axial point spread function (PSF) was obtained as described previously [19,31,67]. Briefly, an XYZ scan was performed through a single 27 nm bead and the maximum projection in the xy-plane was fit to the Gaussian function using Igor Pro software. We obtained the full width at half maximum (FWHM) values for x and y-width of 268 and 273 nm, respectively, in the lateral (x-y plane) and for y-z width of 561 nm in the axial (y-z axis) resolution.

Photobleaching. We minimized photobleaching and phototoxicity during live-cell scanning by using fast scan speed (10 microsec/pixel), low laser intensity (0.01–0.06% of maximum), and low pixel density (frame size, 256 × 256 pixels). We estimated photobleaching using x-t line scans of Cal520HA or Cal520LA and TAMRA-RBP in the absence of stimulation, with the same imaging parameters used for experimental samples.

Data analysis. Quantitative FluoView x-t scans were analyzed initially with ImageJ software (imagej.nih.gov) and subsequently with Igor Pro software (Wavemetrics, Portland OR) using custom-written curve fitting or with Imaris 9.9 software (Version 9.9.0; Bitplane, Zurich, Switzerland). Data from PatchMaster software were initially exported to Microsoft Excel (Version 16.81) for normalizing and averaging and exported from MS Excel to Igor Pro (Version 9.05) for curve fitting and production of the final figures.

Analysis of x-y scan data. We analyzed the rate of loading the TAMRA-RBP and Ca^{2+} indicator into the BPC terminal with ImageJ software by placing a square region of interest (ROI; 5 x 5 μm) and using a Plot z-axis profile function to obtain spatially averaged TAMRA-RBP and Ca^{2+} indicator fluorescence as a function of time. The rising phase of TAMRA-RBP and Ca^{2+} indicator fluorescence was obtained by fitting the rising to the peak to the single exponential function using the curve fitting function in Igor Pro 9 software. The rate of the exponential function is defined as the rate of fluorescence loading to the terminal.

Analysis of x-t scan data.

X-axis profile. To identify the Ca^{2+} signals specific to the ribbon location, we fit x-axis intensity profiles with the equation $f(x) = s(x) + g(x)$, where $s(x)$ is a sigmoid function that describes the transition from intracellular to extracellular background fluorescence at the edge of the cell, given by $s(x) = b - (c/(1-\exp((x_{1/2}-x)/d)))$, and $g(x)$ is a Gaussian function that represents the fluorescence of RBP, given by $g(x) = a(\exp(-(x-x0)^2/w^2))$, as described [68]. The parameters $x_{1/2}$ and x_0 were taken as the x-axis positions of the plasma membrane and the fluorescence emitter, respectively. While parameter b is intracellular background fluorescence, c is extracellular background fluorescence, d is the slope of the sigmoid, a is the peak amplitude of emitter fluorescence, and w is $\sqrt{2}$* the standard deviation of the Gaussian function, in practice, the latter parameters were highly constrained by the data or by the measured PSF, leaving only $x_{1/2}$ and x_0 as free parameters in the fitting.

T-axis profile. The temporal profiles of the Cal520, Cal520-RBP, and TAMRA-RBP signals were determined by analyzing the time-axis profile of the x-t line scan to obtain the kinetics of the Ca^{2+} transient with respect to the ribbon. We determined the baseline kinetics by averaging the fluorescence obtained immediately before depolarization. The timing of depolarization and the amplitude of the Ca^{2+} current was obtained from the PatchMaster software. The rising phase of the Ca^{2+} transient was fit with the sigmoid function, the peak of which is referred to as the peak amplitude Ca^{2+} transient.

We used this baseline profile of ribbon-proximal Ca^{2+} signals to distinguish signals proximal or distal to the ribbon despite the distance between these two signals being within the PSF. For example, the ribbon-proximal signals were obtained by averaging 5 pixels of the temporal profile of the Cal520, Cal520-RBP, and

TAMRA-RBP signals between the $x_{1/2}$ and x_0 values obtained in the x-axis profile. The distal profile was obtained similarly but was 5-pixels after x_0 towards the cytoplasm.

Quantifying the rise-time of the Ca^{2+} transients. The rise-time of the fluoresence transients (**Figs. 2C and 3C**) was defined as the time to reach half-maximal value from the start of the stimulation, after subtracting its baseline. It was determined by fitting a hyperbolic function with an argument shifted by a constant value β, which serves as one of two free parameter of the fit, along with the argument scale factor α characterizing the steepness of the rising phase of the signal:

$$f(t) = F_{peak} [\tanh(\alpha(t - \beta)) + C] / [\tanh(\alpha(t_{peak} - \beta)) + C].$$

The constant $C = \tanh(\alpha^*\beta)$ ensures that $f(0) = 0$ at the start of the stimulation, $t = 0$. This fitting function reaches its peak value F_{peak} at $t = t_{peak}$, as determined from the averaged fluorescence trace. The sign of the argument shift β controls the shape of the signal near $t = 0$: $\beta < 0$ corresponds to a signal which is concave downward (i.e. very rapid onset), while $\beta > 0$ corresponds to a signal which is concave upward near $t = 0$ (i.e. gradual rise). Therefore, this function provides a more flexible functional relationship than the Hill function or the standard sigmoidal function.

Experimental design and statistical methods. We did not use any statistical methods to determine the sample size prior to experiments. Mean value variances were reported as ± the standard error of the mean (SEM). The statistical significance of differences in average amplitudes of Ca^{2+} current, capacitance, synaptic ribbon size and number, and Ca^{2+} transients were assessed using unpaired, two-tailed t-tests with unequal variance using R Studio (Version 2023.09.0+463) and Igor Pro software.

Amplitude analysis for Figure 9. Amplitude data were processed and analyzed using R Studio software (Version 2023.09.0+463). The data were divided into two groups, that of individual cells and of multiple cells, and analyzed as follows. Multiple individual cells from each condition (proximal 10 mM EGTA Cal520LA-RBP and distal 10 mM EGTA Cal520LA-RBP) were analyzed to compare the variability between the Ca^{2+} amplitude measurements of the ribbons from each cell. Having verified the normality of the data to ensure the validity of the statistical test, we used one-way ANOVA and Tukey's honest significant difference test to assess the

specific statistical differences between ribbons. To compare the variability between the amplitude measurements of different cells, we compared readings for various cells. If there were multiple measurements for a single ribbon in a specific cell, those readings were averaged. In this case, the normality of the data was again verified and Welch's ANOVA was employed to assess the between-group differences as it does not assume homogeneity of variance, with the Games-Howell post-hoc test being used to understand the specific differences between cells.

Computational modeling of Ca^{2+} dynamics: Spatio-temporal Ca^{2+} dynamics is simulated in a volume shown in **Fig. 9**, which is a 3D box of dimensions (1.28 x 1.28 x 1.1) μm^3. Assuming an approximately spherical bouton of diameter 5μm and an average of 36 ribbons per terminal, one obtains synaptic volume per ribbon of 1.81 μm^3, which matches the volume of our box domain. Ribbon serves as an obstacle to Ca^{2+} and buffer diffusion, and has an ellipsoidal shape with semi-axis of 190nm along the Y- and Z-axes (for a total height of 380nm), and a semi-axis of 70 nm along the X-axis. It is attached to the plasma membrane by a thin ridge (arciform density) of dimensions 60x30x30 nm. Ca^{2+} ions enter through 4 channels (or clusters of channels) at the base of the ribbon indicated by black disks in **Fig. 6**, forming a square with a side length of 80 nm; this highly simplified channel arrangement is sufficient to capture the level of detail in spatial [Ca^{2+}] distribution that we seek to resolve. Each of the four clusters admits a quarter of the total Ca^{2+} current. Ca^{2+} current values and current pulse durations are listed in **Fig. 7**. Although the actual distribution of Ca^{2+} channels is more heterogeneous, channels close to the ribbon play a greater role in neurotransmitter release [2].

The simulation includes a single dominant Ca^{2+} buffer with molecules possessing a single Ca^{2+} ion binding site. We assume that only immobile buffer is present in a patch-clamped cell, since any mobile buffer would diffuse into recording pipette. Simulations with mobile buffer in an un-patched cell are also provided (**Supplementary Fig. 4**). Buffer parameter values were set to values reported by [7], namely dissociation constant of 2 μM, and total concentration of 1.44 mM (total buffering capacity at rest of 720). We also examine the impact of the assumption on buffer concentration by repeating the simulation with a lower buffering capacity of 100 (total buffer concentration of 200 μM). The Ca^{2+} ion diffusivity is set to 0.22 $\mu m^2/ms$ [71].

To minimize the number of undetermined parameters, we assumed the same parameters for the Ca^{2+} clearance on all surfaces, with one high-capacity but lower affinity process simulating Na^+/Ca^{2+} exchangers,

and one lower capacity but higher affinity process simulating Ca^{2+} extrusion by ATPase PMCA and SERCA pumps. We used the Hill coefficient of m=2 for the Ca^{2+} sensitivity of the SERCA pumps on all surfaces except the bottom surface [72], whereas Hill coefficient of m=1 corresponds to PMCA pumps on the bottom surface [73]. Thus, the flux of [Ca^{2+}] across the surface (ions extruded per unit area per unit time) is described by

$$\Phi_{Ca} = D_C\left(\mathbf{n}\cdot\nabla C\right) = \frac{A_{NCX}C}{K_{NCX}+C} + \frac{A_P C^m}{K_P^m + C^m} - \Phi_{Leak},$$

where C is the Ca^{2+} concentration, D_C is the Ca^{2+} diffusivity, and $\boldsymbol{n}\cdot\boldsymbol{\nabla C}$ is the gradient of [Ca^{2+}] normal to the boundary. The constant leak term Φ_{Leak} ensures that the flux is zero at the resting value $[Ca^{2+}]_{rest} = C_0 = 0.1$ μM. The Ca^{2+} clearance rate and affinity parameters for the pumps and exchangers are listed in **Supplementary Table 1**. We note however that the density of Na^+-Ca^{2+} exchangers and PMCA/SERCA pumps are rough estimates and have a significant effect on results only for longer stimulation durations of over 100-200 ms. Reaction-diffusion equations for [Ca^{2+}] and buffer are solved numerically using Calcium Calculator software version 6.10.7 [74,75].

Serial block-face scanning electron microscopy (SBF-SEM). The eyecups of adult (16 ~20-month-old) zebrafish were dissected in bicarbonate-buffered Ames' medium and, after removing the lens, the eyecups were fixed in 4% glutaraldehyde in 0.1 M sodium-cacodylate buffer at RT for one hour, followed by overnight fixation at 4°C. Thereafter, samples were treated to generate blocks for serial block face scanning electron microscopy (SBF-SEM) according to the published protocol [76], in this case using Zeiss 3-View SBF-SEM. Multiple 35 μm montages were acquired at a 5nm X-Y resolution and a 50nm Z resolution across the entire retina from the outer (photoreceptor) layer to the inner (ganglion) cell layer. Images were inspected visually and structures of interest were traced using the TrakEM plug-in in ImageJ software (NIH/Fiji), as described below.

Analysis of serial block-face scanning electron microscopy images. SBF-SEM image stacks of the zebrafish retina were imported, aligned, visualized, and analyzed using the TrakEM plugin (version 1.5h) in ImageJ software (NIH). RBC1 rod bipolar cells were identified based on their characteristic morphology and 4-7 μm size, as described [42]. Rod BPCs, synaptic ribbons, pre-synaptic membranes, and the area of the ribbon

touching the plasma membrane were traced, painted using the TrakEM brush features, and rendered in 3D for structural visualization. The area of the synaptic ribbon touching the rod bipolar cell membrane was quantified using the measuring tools in ImageJ and images were prepared using Adobe Photoshop software (version 25.9).

Acknowledgements:

This research was funded by the National Institutes of Health (NIH) National Eye Institute (NEI), award numbers R01EY030863, 3R01EY030863-02S1, and 3R01EY030863-03S1, and a UTHSC College of Medicine Faculty Research Growth Award (to TV), R01 EY032396, P30EY026878, R01NS122388 (DZ), and a University of Wisconsin-Madison (UW2020) WARF discovery award (to MH) which funded the acquisition of the 3D view serial block-face electron microscope. We would like to acknowledge the UW Madison School of Medicine electron microscopy facility for processing and imaging samples and thank Dr. Alex Dopico, the Van Vleet Chair of Excellence and Professor in the Department of Pharmacology, Addiction Science, and Toxicology, UTHSC, for critical reading, and Dr. Kyle Johnson Moore in the UTHSC Office of Research for editing the manuscript.

Author Contributions

Conceptualization, D.Z. and T.V.; Methodology and Investigation, N.R., A.S.; Data analysis, N.R., A.S., J.B., M.H., T.V.; Computational modeling, V.M.; Visualization, J.B., M.H., V.M., T.V.; Writing - Original Draft, N.R., T.V.; Writing-Review & Editing, all authors; Funding, M.H., D.Z., T.V.; Supervision and Project administration, T.V.

Competing Interests

The authors declare no conflict of interest.

References

1. Matthews, G., and Fuchs, P. (2010). The diverse roles of ribbon synapses in sensory neurotransmission. Nat Rev Neurosci *11*, 812-822. 10.1038/nrn2924.
2. Moser, T., Grabner, C.P., and Schmitz, F. (2020). Sensory Processing at Ribbon Synapses in the Retina and the Cochlea. Physiol Rev *100*, 103-144. 10.1152/physrev.00026.2018.
3. Regus-Leidig, H., and Brandstätter, J.H. (2012). Structure and function of a complex sensory synapse. Acta Physiol (Oxf) *204*, 479-486. 10.1111/j.1748-1716.2011.02355.x.
4. Snellman, J., Mehta, B., Babai, N., Bartoletti, T.M., Akmentin, W., Francis, A., Matthews, G., Thoreson, W., and Zenisek, D. (2011). Acute destruction of the synaptic ribbon reveals a role for the ribbon in vesicle priming. Nat Neurosci *14*, 1135-1141. 10.1038/nn.2870.
5. Zanazzi, G., and Matthews, G. (2009). The molecular architecture of ribbon presynaptic terminals. Mol Neurobiol *39*, 130-148. 10.1007/s12035-009-8058-z.
6. Oesch, N.W., and Diamond, J.S. (2011). Ribbon synapses compute temporal contrast and encode luminance in retinal rod bipolar cells. Nat Neurosci *14*, 1555-1561. 10.1038/nn.2945.
7. Burrone, J., Neves, G., Gomis, A., Cooke, A., and Lagnado, L. (2002). Endogenous calcium buffers regulate fast exocytosis in the synaptic terminal of retinal bipolar cells. Neuron *33*, 101-112.
8. Coggins, M., and Zenisek, D. (2009). Evidence that exocytosis is driven by calcium entry through multiple calcium channels in goldfish retinal bipolar cells. J Neurophysiol *101*, 2601-2619. 10.1152/jn.90881.2008.
9. Graydon, C.W., Cho, S., Li, G.L., Kachar, B., and von Gersdorff, H. (2011). Sharp Ca(2)(+) nanodomains beneath the ribbon promote highly synchronous multivesicular release at hair cell synapses. J Neurosci *31*, 16637-16650. 10.1523/JNEUROSCI.1866-11.2011.
10. Jarsky, T., Tian, M., and Singer, J.H. (2010). Nanodomain control of exocytosis is responsible for the signaling capability of a retinal ribbon synapse. J Neurosci *30*, 11885-11895. 10.1523/JNEUROSCI.1415-10.2010.
11. Mennerick, S., and Matthews, G. (1996). Ultrafast exocytosis elicited by calcium current in synaptic terminals of retinal bipolar neurons. Neuron *17*, 1241-1249.
12. Singer, J.H., and Diamond, J.S. (2003). Sustained Ca2+ entry elicits transient postsynaptic currents at a retinal ribbon synapse. J Neurosci *23*, 10923-10933. 10.1523/jneurosci.23-34-10923.2003.
13. Snellman, J., Zenisek, D., and Nawy, S. (2009). Switching between transient and sustained signalling at the rod bipolar-AII amacrine cell synapse of the mouse retina. J Physiol *587*, 2443-2455. 10.1113/jphysiol.2008.165241.
14. von Gersdorff, H., and Matthews, G. (1994). Dynamics of synaptic vesicle fusion and membrane retrieval in synaptic terminals. Nature *367*, 735-739. 10.1038/367735a0.
15. Burrone, J., and Lagnado, L. (2000). Synaptic depression and the kinetics of exocytosis in retinal bipolar cells. J Neurosci *20*, 568-578.
16. Kobayashi, K., and Tachibana, M. (1995). Ca2+ regulation in the presynaptic terminals of goldfish retinal bipolar cells. J Physiol *483 (Pt 1)*, 79-94. 10.1113/jphysiol.1995.sp020569.
17. Wan, Q.F., Nixon, E., and Heidelberger, R. (2012). Regulation of presynaptic calcium in a mammalian synaptic terminal. J Neurophysiol *108*, 3059-3067. 10.1152/jn.00213.2012.
18. Zenisek, D., and Matthews, G. (2000). The role of mitochondria in presynaptic calcium handling at a ribbon synapse. Neuron *25*, 229-237. 10.1016/s0896-6273(00)80885-5.
19. Vaithianathan, T., and Matthews, G. (2014). Visualizing synaptic vesicle turnover and pool refilling driven by calcium nanodomains at presynaptic active zones of ribbon synapses. Proc Natl Acad Sci U S A *111*, 8655-8660. 10.1073/pnas.1323962111.
20. Francis, A.A., Mehta, B., and Zenisek, D. (2011). Development of new peptide-based tools for studying synaptic ribbon function. J Neurophysiol *106*, 1028-1037. 10.1152/jn.00255.2011.

21. Grassmeyer, J.J., and Thoreson, W.B. (2017). Synaptic Ribbon Active Zones in Cone Photoreceptors Operate Independently from One Another. Front Cell Neurosci *11*, 198. 10.3389/fncel.2017.00198.
22. Ohn, T.L., Rutherford, M.A., Jing, Z., Jung, S., Duque-Afonso, C.J., Hoch, G., Picher, M.M., Scharinger, A., Strenzke, N., and Moser, T. (2016). Hair cells use active zones with different voltage dependence of Ca2+ influx to decompose sounds into complementary neural codes. Proc Natl Acad Sci U S A *113*, E4716-4725. 10.1073/pnas.1605737113.
23. Frank, T., Khimich, D., Neef, A., and Moser, T. (2009). Mechanisms contributing to synaptic Ca2+ signals and their heterogeneity in hair cells. Proc Natl Acad Sci U S A *106*, 4483-4488. 10.1073/pnas.0813213106.
24. Éltes, T., Kirizs, T., Nusser, Z., and Holderith, N. (2017). Target Cell Type-Dependent Differences in Ca(2+) Channel Function Underlie Distinct Release Probabilities at Hippocampal Glutamatergic Terminals. J Neurosci *37*, 1910-1924. 10.1523/jneurosci.2024-16.2017.
25. Trexler, E.B., Li, W., and Massey, S.C. (2005). Simultaneous contribution of two rod pathways to AII amacrine and cone bipolar cell light responses. J Neurophysiol *93*, 1476-1485. 10.1152/jn.00597.2004.
26. Ke, J.B., Wang, Y.V., Borghuis, B.G., Cembrowski, M.S., Riecke, H., Kath, W.L., Demb, J.B., and Singer, J.H. (2014). Adaptation to background light enables contrast coding at rod bipolar cell synapses. Neuron *81*, 388-401. 10.1016/j.neuron.2013.10.054.
27. Euler, T., Haverkamp, S., Schubert, T., and Baden, T. (2014). Retinal bipolar cells: elementary building blocks of vision. Nat Rev Neurosci *15*, 507-519. 10.1038/nrn3783.
28. Liberman, L.D., Wang, H., and Liberman, M.C. (2011). Opposing gradients of ribbon size and AMPA receptor expression underlie sensitivity differences among cochlear-nerve/hair-cell synapses. J Neurosci *31*, 801-808. 10.1523/jneurosci.3389-10.2011.
29. Merchan-Perez, A., and Liberman, M.C. (1996). Ultrastructural differences among afferent synapses on cochlear hair cells: correlations with spontaneous discharge rate. J Comp Neurol *371*, 208-221. 10.1002/(sici)1096-9861(19960722)371:2<208::Aid-cne2>3.0.Co;2-6.
30. Zenisek, D., Horst, N.K., Merrifield, C., Sterling, P., and Matthews, G. (2004). Visualizing synaptic ribbons in the living cell. J Neurosci *24*, 9752-9759. 10.1523/JNEUROSCI.2886-04.2004.
31. Vaithianathan, T., Wollmuth, L.P., Henry, D., Zenisek, D., and Matthews, G. (2019). Tracking Newly Released Synaptic Vesicle Proteins at Ribbon Active Zones. iScience *17*, 10-23. 10.1016/j.isci.2019.06.015.
32. Roberts, W.M. (1994). Localization of calcium signals by a mobile calcium buffer in frog saccular hair cells. J Neurosci *14*, 3246-3262. 10.1523/jneurosci.14-05-03246.1994.
33. Naraghi, M., and Neher, E. (1997). Linearized buffered Ca2+ diffusion in microdomains and its implications for calculation of [Ca2+] at the mouth of a calcium channel. J Neurosci *17*, 6961-6973. 10.1523/jneurosci.17-18-06961.1997.
34. Zucker, R.S., and Fogelson, A.L. (1986). Relationship between transmitter release and presynaptic calcium influx when calcium enters through discrete channels. Proc Natl Acad Sci U S A *83*, 3032-3036. 10.1073/pnas.83.9.3032.
35. Datta, P., Gilliam, J., Thoreson, W.B., Janz, R., and Heidelberger, R. (2017). Two Pools of Vesicles Associated with Synaptic Ribbons Are Molecularly Prepared for Release. Biophys J *113*, 2281-2298. 10.1016/j.bpj.2017.08.012.
36. Neves, G., and Lagnado, L. (1999). The kinetics of exocytosis and endocytosis in the synaptic terminal of goldfish retinal bipolar cells. J Physiol *515 (Pt 1)*, 181-202. 10.1111/j.1469-7793.1999.181ad.x.
37. von Gersdorff, H., and Matthews, G. (1997). Depletion and replenishment of vesicle pools at a ribbon-type synaptic terminal. J Neurosci *17*, 1919-1927.
38. Zhou, Z.Y., Wan, Q.F., Thakur, P., and Heidelberger, R. (2006). Capacitance measurements in the mouse rod bipolar cell identify a pool of releasable synaptic vesicles. J Neurophysiol *96*, 2539-2548. 10.1152/jn.00688.2006.

39. Neves, G., and Lagnado, L. (1999). The retina. Curr Biol *9*, R674-677. 10.1016/s0960-9822(99)80436-9.
40. Zenisek, D., Steyer, J.A., and Almers, W. (2000). Transport, capture and exocytosis of single synaptic vesicles at active zones. Nature *406*, 849-854. 10.1038/35022500.
41. Hellevik, A.M., Mardoum, P., Hahn, J., Kölsch, Y., D'Orazi, F.D., Suzuki, S.C., Godinho, L., Lawrence, O., Rieke, F., Shekhar, K., et al. (2024). Ancient origin of the rod bipolar cell pathway in the vertebrate retina. Nat Ecol Evol *8*, 1165-1179. 10.1038/s41559-024-02404-w.
42. Hellevik, A.M., Mardoum, P., Hahn, J., Kölsch, Y., D'Orazi, F.D., Suzuki, S.C., Godinho, L., Lawrence, O., Rieke, F., Shekhar, K., et al. (2023). Ancient origin of the rod bipolar cell pathway in the vertebrate retina. bioRxiv. 10.1101/2023.09.12.557433.
43. Heidelberger, R., Heinemann, C., Neher, E., and Matthews, G. (1994). Calcium dependence of the rate of exocytosis in a synaptic terminal. Nature *371*, 513-515. 10.1038/371513a0.
44. Grynkiewicz, G., Poenie, M., and Tsien, R.Y. (1985). A new generation of Ca2+ indicators with greatly improved fluorescence properties. J Biol Chem *260*, 3440-3450.
45. Neef, J., Urban, N.T., Ohn, T.L., Frank, T., Jean, P., Hell, S.W., Willig, K.I., and Moser, T. (2018). Quantitative optical nanophysiology of Ca(2+) signaling at inner hair cell active zones. Nat Commun *9*, 290. 10.1038/s41467-017-02612-y.
46. Uto, A., Arai, H., and Ogawa, Y. (1991). Reassessment of Fura-2 and the ratio method for determination of intracellular Ca2+ concentrations. Cell Calcium *12*, 29-37. 10.1016/0143-4160(91)90082-p.
47. Woehler, A., Lin, K.H., and Neher, E. (2014). Calcium-buffering effects of gluconate and nucleotides, as determined by a novel fluorimetric titration method. J Physiol *592*, 4863-4875. 10.1113/jphysiol.2014.281097.
48. Shirakawa, H., and Miyazaki, S. (2004). Blind spectral decomposition of single-cell fluorescence by parallel factor analysis. Biophys J *86*, 1739-1752. 10.1016/s0006-3495(04)74242-3.
49. Midorikawa, M., Tsukamoto, Y., Berglund, K., Ishii, M., and Tachibana, M. (2007). Different roles of ribbon-associated and ribbon-free active zones in retinal bipolar cells. Nat Neurosci *10*, 1268-1276. 10.1038/nn1963.
50. Zenisek, D. (2008). Vesicle association and exocytosis at ribbon and extraribbon sites in retinal bipolar cell presynaptic terminals. Proc Natl Acad Sci U S A *105*, 4922-4927. 10.1073/pnas.0709067105.
51. Chen, M., Van Hook, M.J., Zenisek, D., and Thoreson, W.B. (2013). Properties of ribbon and non-ribbon release from rod photoreceptors revealed by visualizing individual synaptic vesicles. J Neurosci *33*, 2071-2086. 10.1523/jneurosci.3426-12.2013.
52. Mehta, B., Ke, J.B., Zhang, L., Baden, A.D., Markowitz, A.L., Nayak, S., Briggman, K.L., Zenisek, D., and Singer, J.H. (2014). Global Ca2+ signaling drives ribbon-independent synaptic transmission at rod bipolar cell synapses. J Neurosci *34*, 6233-6244. 10.1523/jneurosci.5324-13.2014.
53. Eisner, D., Neher, E., Taschenberger, H., and Smith, G. (2023). Physiology of intracellular calcium buffering. Physiol Rev *103*, 2767-2845. 10.1152/physrev.00042.2022.
54. Neher, E. (1998). Usefulness and limitations of linear approximations to the understanding of Ca++ signals. Cell Calcium *24*, 345-357. 10.1016/s0143-4160(98)90058-6.
55. Matthews, E.A., and Dietrich, D. (2015). Buffer mobility and the regulation of neuronal calcium domains. Front Cell Neurosci *9*, 48. 10.3389/fncel.2015.00048.
56. Babai, N., Morgans, C.W., and Thoreson, W.B. (2010). Calcium-induced calcium release contributes to synaptic release from mouse rod photoreceptors. Neuroscience *165*, 1447-1456. 10.1016/j.neuroscience.2009.11.032.
57. Gomis, A., Burrone, J., and Lagnado, L. (1999). Two actions of calcium regulate the supply of releasable vesicles at the ribbon synapse of retinal bipolar cells. J Neurosci *19*, 6309-6317.
58. Johnson, S.L., Forge, A., Knipper, M., Munkner, S., and Marcotti, W. (2008). Tonotopic variation in the calcium dependence of neurotransmitter release and vesicle pool replenishment at mammalian auditory ribbon synapses. J Neurosci *28*, 7670-7678. 10.1523/JNEUROSCI.0785-08.2008.

59. Singer, J.H., and Diamond, J.S. (2006). Vesicle depletion and synaptic depression at a mammalian ribbon synapse. J Neurophysiol *95*, 3191-3198. 10.1152/jn.01309.2005.
60. von Gersdorff, H., Vardi, E., Matthews, G., and Sterling, P. (1996). Evidence that vesicles on the synaptic ribbon of retinal bipolar neurons can be rapidly released. Neuron *16*, 1221-1227. 10.1016/s0896-6273(00)80148-8.
61. Martinez-Dunst, C., Michaels, R.L., and Fuchs, P.A. (1997). Release sites and calcium channels in hair cells of the chick's cochlea. J Neurosci *17*, 9133-9144. 10.1523/jneurosci.17-23-09133.1997.
62. von Gersdorff, H., and Matthews, G. (1994). Inhibition of endocytosis by elevated internal calcium in a synaptic terminal. Nature *370*, 652-655. 10.1038/370652a0.
63. Shrestha, A.P., Rameshkumar, N., Boff, J.M., Rajmanna, R., Chandrasegaran, T., Frederick, C.E., Zenisek, D., and Vaithianathan, T. (2023). The Effects of Aging on Rod Bipolar Cell Ribbon Synapses. Cells *12*. 10.3390/cells12192385.
64. Kobayashi, K., Sakaba, T., and Tachibana, M. (1995). Potentiation of Ca2+ transients in the presynaptic terminals of goldfish retinal bipolar cells. J Physiol *482 (Pt 1)*, 7-13. 10.1113/jphysiol.1995.sp020495.
65. Micci, M.A., and Christensen, B.N. (1996). Distribution of the inositol trisphosphate receptor in the catfish retina. Brain Res *720*, 139-147. 10.1016/0006-8993(95)01463-2.
66. Koulen, P., Wei, J., Madry, C., Liu, J., and Nixon, E. (2005). Differentially distributed IP3 receptors and Ca2+ signaling in rod bipolar cells. Invest Ophthalmol Vis Sci *46*, 292-298. 10.1167/iovs.04-0939.
67. Shrestha, A.P., and Vaithianathan, T. (2022). Tracking the dynamics of single fused synaptic vesicle proteins from a single ribbon active zone in zebrafish retinal bipolar cells. STAR Protoc *3*, 101107. 10.1016/j.xpro.2021.101107.
68. Vaithianathan, T., Henry, D., Akmentin, W., and Matthews, G. (2016). Nanoscale dynamics of synaptic vesicle trafficking and fusion at the presynaptic active zone. Elife *5*. 10.7554/eLife.13245.
69. Shrestha, A.P., Saravanakumar, A., Konadu, B., Madireddy, S., Gibert, Y., and Vaithianathan, T. (2022). Embryonic Hyperglycemia Delays the Development of Retinal Synapses in a Zebrafish Model. Int J Mol Sci *23*. 10.3390/ijms23179693.
70. Vaithianathan, T., Zanazzi, G., Henry, D., Akmentin, W., and Matthews, G. (2013). Stabilization of spontaneous neurotransmitter release at ribbon synapses by ribbon-specific subtypes of complexin. J Neurosci *33*, 8216-8226. 10.1523/JNEUROSCI.1280-12.2013.
71. Allbritton, N.L., Meyer, T., and Stryer, L. (1992). Range of messenger action of calcium ion and inositol 1,4,5-trisphosphate. Science *258*, 1812-1815.
72. Lytton, J., Westlin, M., Burk, S.E., Shull, G.E., and MacLennan, D.H. (1992). Functional comparisons between isoforms of the sarcoplasmic or endoplasmic reticulum family of calcium pumps. J Biol Chem *267*, 14483-14489.
73. Brini, M. (2009). Plasma membrane Ca(2+)-ATPase: from a housekeeping function to a versatile signaling role. Pflugers Arch *457*, 657-664. 10.1007/s00424-008-0505-6.
74. Matveev, V., Sherman, A., and Zucker, R.S. (2002). New and corrected simulations of synaptic facilitation. Biophys J *83*, 1368-1373. 10.1016/S0006-3495(02)73907-6.
75. Matveev, V. (2023). CalC (Calcium Calculator) simulation software, release version 6.10.7. https://github.com/mvvik/CalC-simple-buffer.
76. Della Santina, L., Kuo, S.P., Yoshimatsu, T., Okawa, H., Suzuki, S.C., Hoon, M., Tsuboyama, K., Rieke, F., and Wong, R.O.L. (2016). Glutamatergic Monopolar Interneurons Provide a Novel Pathway of Excitation in the Mouse Retina. Curr Biol *26*, 2070-2077. 10.1016/j.cub.2016.06.016.

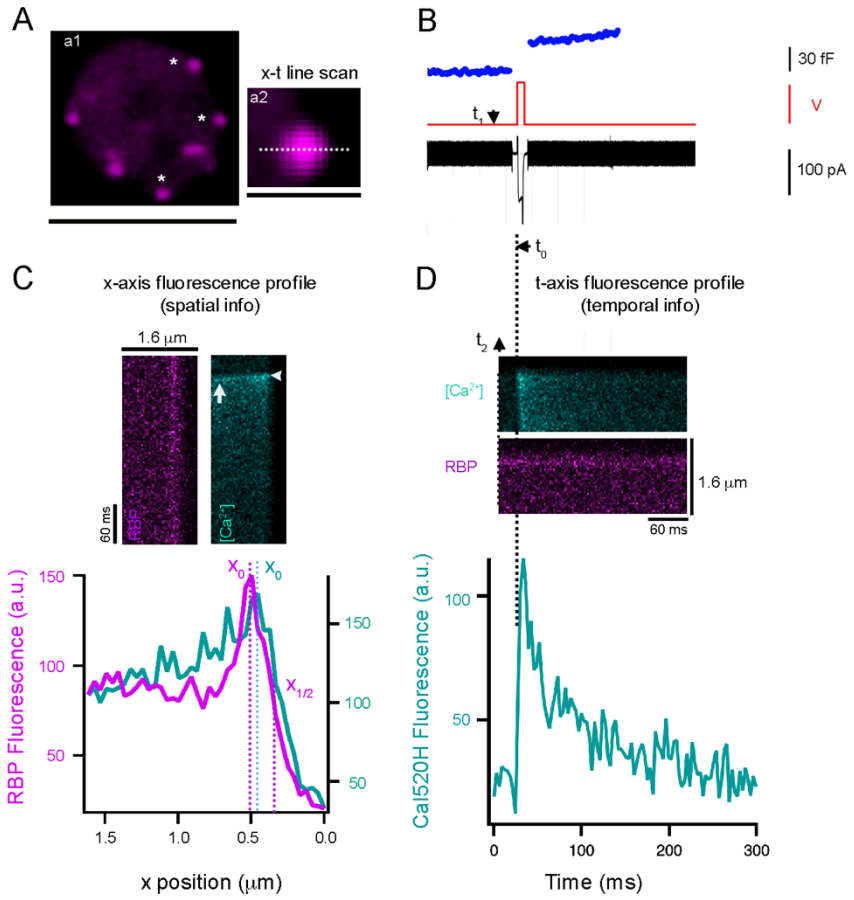

Fig 1. Nanophysiology approach to unveil spatiotemporal properties of local Ca^{2+} signaling in retinal bipolar cell terminals.

A. Left panel. Single projection from a series of confocal optical sections through a zebrafish rod BPC synaptic terminal. A synaptic terminal was voltage-clamped using a whole-cell pipette with an internal solution containing TAMRA- RBP (magenta) to label synaptic ribbons. RBP fluorescence was concentrated at ribbons and also filled the entire terminal, allowing visualization of the terminal border. Experiments were carried out on ribbons that could be distinguished from adjacent ribbons (white asterisks). Scale, 5 µm. **Right panel**, Close-up view of a single synaptic ribbon. The outside of the cell is to the right, and x-t scan lines (dotted lines) were positioned perpendicular to the plasma membrane, extending from the intracellular side of the ribbon to the extracellular space. The resulting x-t raster plots were used to measure the fluorescence intensity profiles of RBP (magenta) and the Ca^{2+} transient (cyan; Cal520HA) shown in panels **C** and **D**. Scale, 1.6 µm.

B. Voltage-clamp recording of a rod bipolar cell terminal. Terminals were held at -65 mV and stepped to 0 mV (t_0) for 10 ms (red) to evoke a brief Ca^{2+} current (black). A sinusoidal voltage stimulus was used to monitor membrane capacitance (blue). A typical experiment began with a voltage command (V_H= -65 mV) and a TTL pulse generated by the Patch Master software (t_1) triggers image acquisition (t_2). t_0 is the time of depolarization.

C. Illustration of the approach used to obtain the spatial location of Ca^{2+} signals with respect to the ribbon. **Upper panel**. Example of an x-t raster plot that is oriented to illustrate the x-axis intensity profiles of RBP (magenta) and Ca^{2+} signal (cyan) fluorescence during a brief depolarization. **Lower panel**. Fluorescence intensity profiles along the x-axis for RBP (magenta) and Ca^{2+} signals (cyan) were fit with a Sigmoid-Gaussian function [1]. The centroid (x-axis position) of the RBP (magenta) and Ca^{2+} signals (cyan) were taken as the peak of the Gaussian fit (x_0). The parameter $x_{1/2}$ (dotted magenta line) from the Sigmoid fit to the RBP fluorescence (magenta trace) was used to estimate the location of the plasma membrane.

D. Upper panel. The x-t raster plot shown was from the same recording as in **panel C** but re-oriented to demonstrate the t-axis intensity profiles of RBP (magenta) and Ca^{2+} transient (cyan). **Lower panel.** Temporal intensity profile of the Ca^{2+} transient.

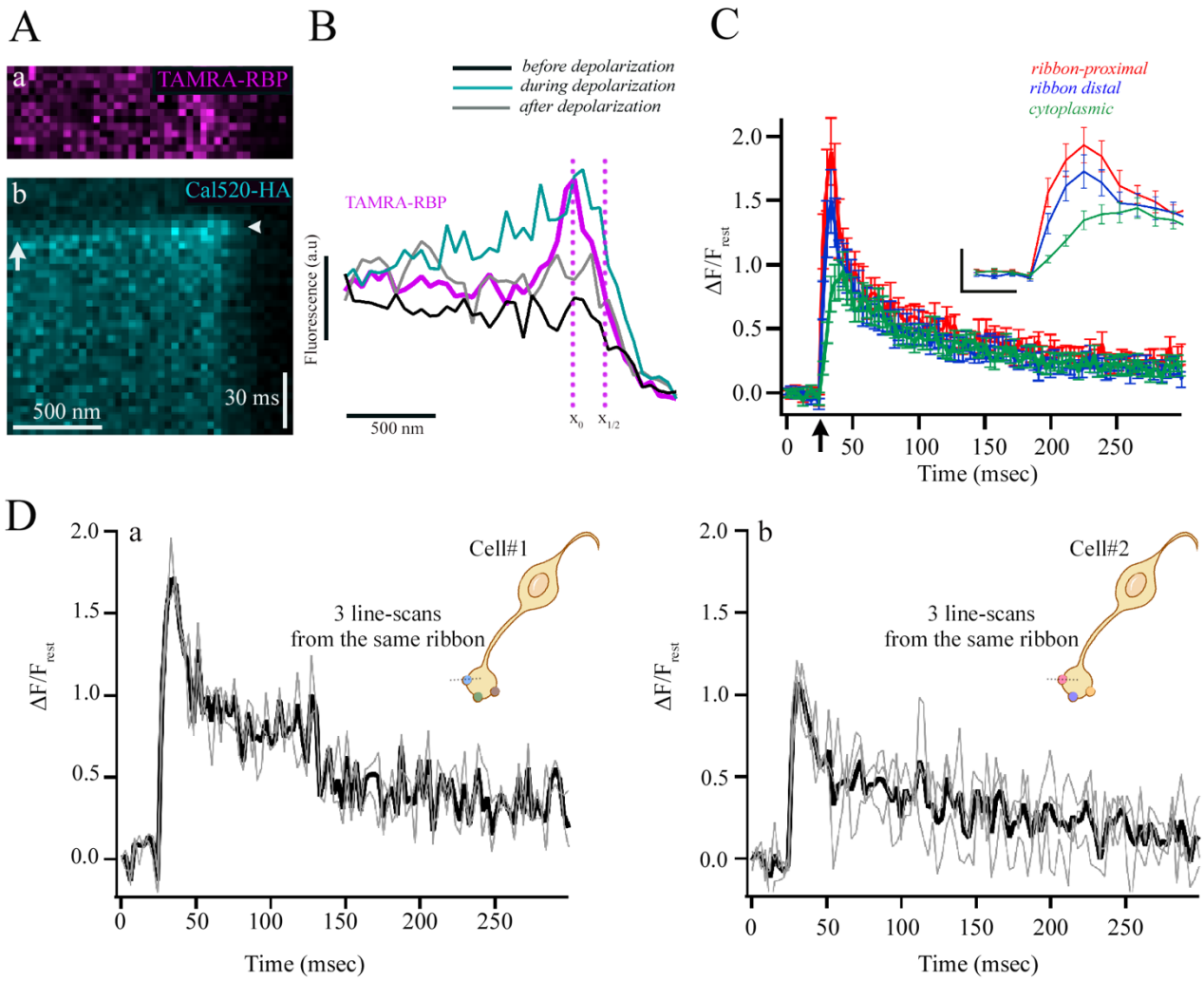

Fig. 2. Variability in Ca^{2+} transients in response to brief stimuli.

Aa-b. X-t plots show the fluorescence intensity as a function of distance (horizontal axis) and time (vertical axis) of (**Aa**) TAMRA-RBP and (**Ab**) Cal520HA at a ribbon location, as indicated in **Fig. 1Aa2**. The extracellular space is the darker region at the left edge of each plot. The white arrowhead and arrow in **panel Ab** indicate the onset of the 10 ms stimulus and the rise time of cytoplasmic Cal520HA fluorescence, respectively.

B. Intensity profiles of TAMRA-RBP (magenta) and Cal520 (cyan) were taken from the images in **panels Aa-b**. The position of the ribbon along the scanned line is indicated by that of the TAMRA-RBP staining. The fluorescence of Cal520HA is shown before (solid black line), during (cyan line), and after (gray line) depolarization. The x-axis position of TAMRA-RBP was taken as the peak of the Gaussian fit (x_0, dotted magenta line) and that of the plasma membrane was taken as the parameter $x_{1/2}$ (dotted magenta line) from the fit to the fluorescence profile of the ribbon (magenta traces). Vertical Scale: 50 (Cal520HA) and 70 (TAMRA-RBP).

C. Spatially averaged Cal520 fluorescence as a function of time at ribbon proximal, distal, and cytoplasmic locations from the single ribbon shown in **panel Ab** (n=24 ribbons from 7 different BPCs).

C inset. The temporal profile of events between 10-50 ms are shown in an expanded view for better visualization. Scale bars: vertical, 0.5 ($\Delta F/F_{rest}$); horizontal,10 ms.

Da-b. The average (black trace) of 3 stimuli (gray traces) at a single ribbon active zone/Ca^{2+} microdomain was obtained from two bipolar cells as described in **panels A-C**. Note the amplitude variability between two cells (#1, panel a; and #2, panel b) with similar Ca^{2+} currents.

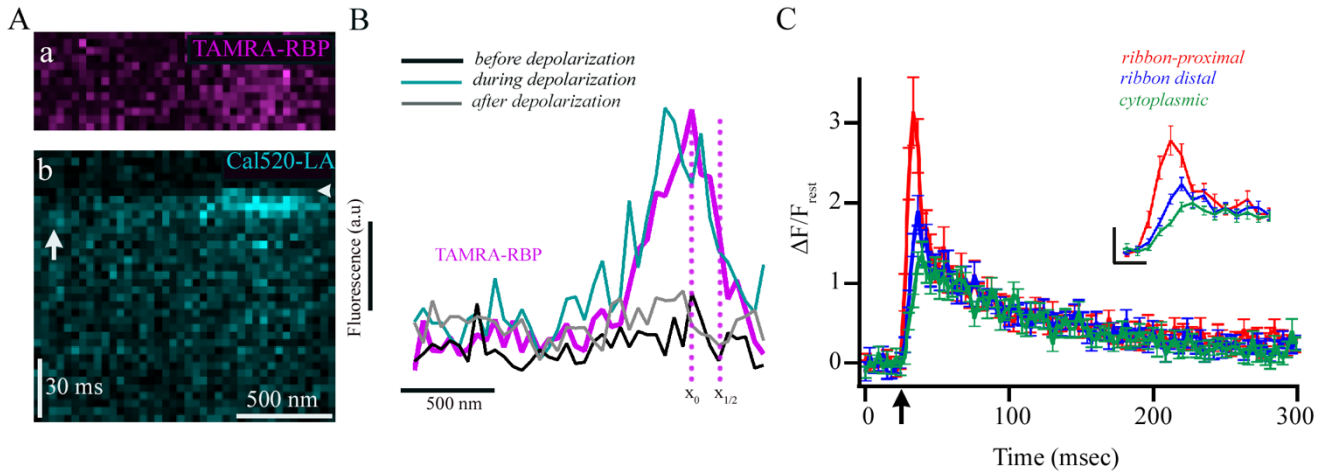

Fig.3 Spatiotemporal properties of Ca^{2+} microdomains control kinetically distinct neurotransmitter release.

Aa-b. (Aa) X-t plots show the fluorescence intensity of RBP-TAMRA (magenta). The outside of the cell is oriented toward the left. (**Ab**) X-t plot of Cal520LA at the onset of the stimulus shows the influx of Ca^{2+} at the membrane (white arrowhead) where Ca^{2+} channels are located. The white arrow shows a slow rise in Cal520LA fluorescence intensity in the cytoplasm.

B. Horizontal intensity profile of fluorescence of RBP (purple) and Cal520LA at time points before (solid black line), during (cyan line), and after (gray line) depolarization. The parameter x_0 is the peak of the Gaussian fit, giving the x-position of the center of the ribbon, and $x_{1/2}$ is the location of the plasma membrane (see Materials and Methods). Vertical Scale: 100 (Cal520LA) and 20 (TAMRA-RBP).

C. Spatially averaged Cal520LA fluorescence as a function of time at ribbon proximal (red), distal (blue), and cytoplasm (green) locations. Data points show the average intensity (± SEM) in each horizontal row of 5 pixels for three 10 ms depolarizations at distinct ribbon locations (see Materials and Methods and **Fig.1**). Fluorescence intensity is normalized with respect to the baseline fluorescence before stimulation, and averaged over all pixels (i.e., over space and time). The arrow indicates the onset of the 10-ms depolarizing stimulus. (n=21 ribbons from 4 different BPCs)

C *inset*. Temporal profile of events between 20-60 ms were expanded for better visualization. Scale bars: vertical, 1 ($\Delta F/F_{rest}$); horizontal, 10 ms.

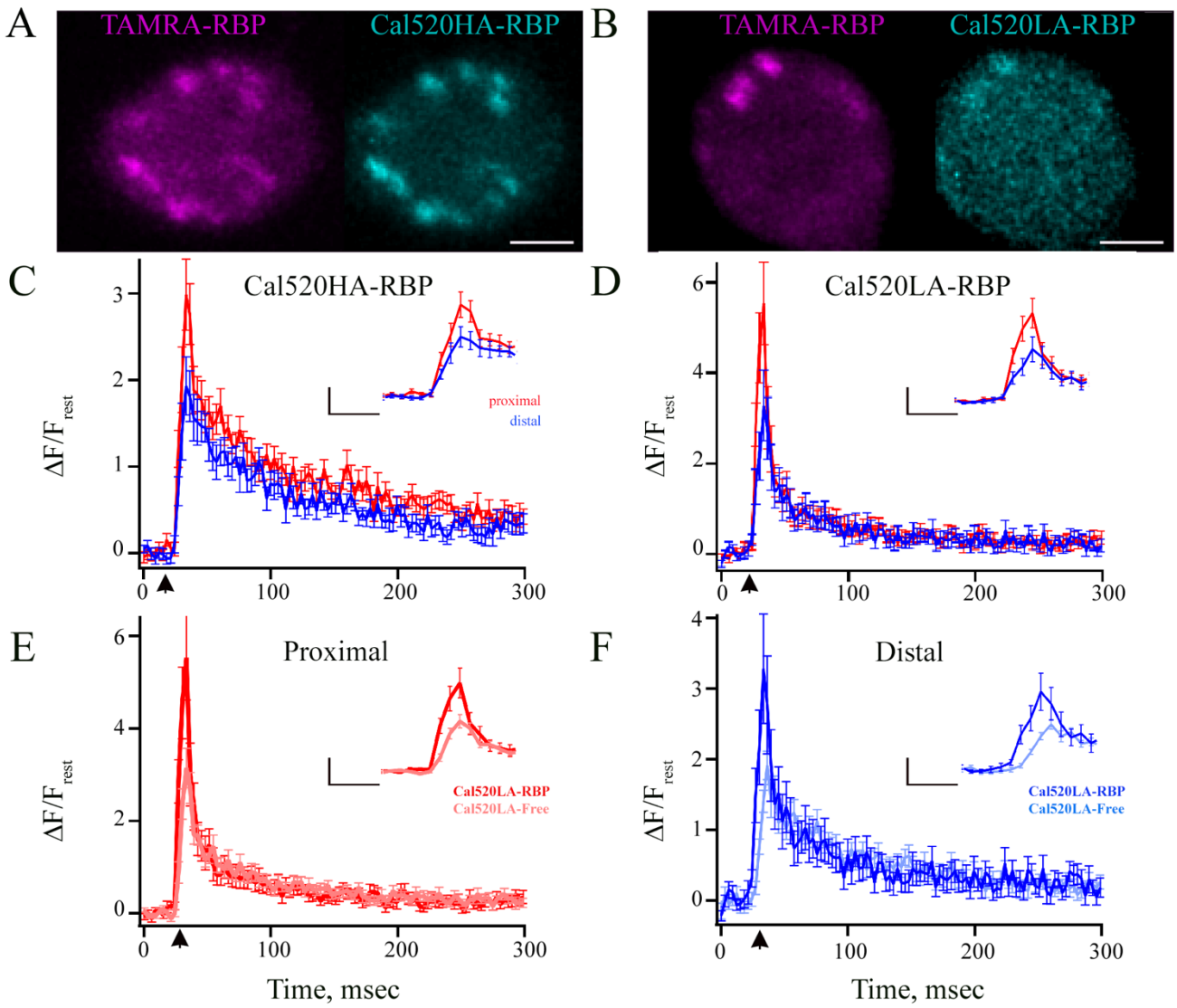

Fig.4. Temporal properties of free and ribeye bound Ca^{2+} indicators.

A-B. Confocal images of the isolated rod bipolar cells that were whole-cell voltage-clamped using an internal solution containing the TAMRA-RBP (magenta) and either (**A**) Cal520HA-RBP (cyan) or (**B**) Cal520LA-RBP (cyan). Note prominent spots in both TAMRA-RBP and ribeye-bound Ca^{2+} indicators (**A**) Cal520HA-RBP (cyan) or (**B**) Cal520LA-RBP, showing the location of the ribbon. Scale bars, 2 μm.

C-D. Spatially averaged fluorescence of (**C**) Cal520HA-RBP (n=19) or (**D**) Cal520LA-RBP (n=30) as a function of time at ribbon proximal (red), and distal (blue) locations. Data points show the average intensity (± SEM) in each horizontal row of five pixels for 10 ms depolarizations at distinct ribbon locations. Fluorescence intensity at the onset of the 10 ms depolarizing stimulus (arrow) was normalized to the baseline fluorescence before stimulation and averaged over all pixels (i.e., over space and time).

C-D inset. Temporal profile of events between 10-50 ms were expanded for better visualization. Scale bars: vertical, 1 ($\Delta F/F_{rest}$, **C inset**) or 2 ($\Delta F/F_{rest}$, **D inset**); horizontal, 10 ms.

E-F. Average fluorescence intensity of (**E**) proximal and (**F**) distal Ca^{2+} signals obtained with Cal520LA-RBP (red, dark blue) and Cal520L-free (pink, light blue).

E-F *inset*. Events between 10-50 ms was expanded for better visualization. Scale bars: vertical, 2 ($\Delta F/F_{rest}$, **E inset**) and 1 ($\Delta F/F_{rest}$, **F inset**); horizontal, 10 ms.

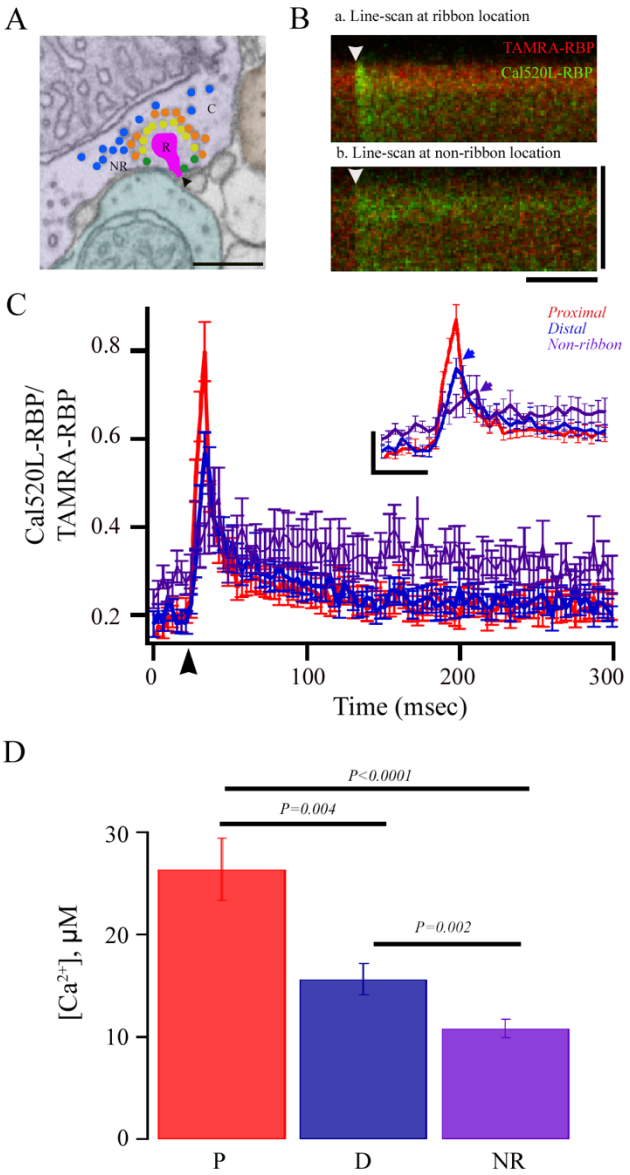

Fig.5. Ca^{2+} signals at synaptic ribbon at different distances from the plasma membrane.

A. Ultrastructure of a zebrafish rod bipolar cell with kinetically distinct vesicle pools, as described in **Supplementary Fig. 2**. UFRP (green vesicles), and RRP (yellow vesicles) are primarily released via ribbon sites (R) at the cytomatrix of the active zone (arrowhead). Recycling pool (RP, orange vesicles) in the cytoplasm (C), likely to be released via non-ribbon (NR) sites. Scale bar: 500 nm.

B. Representative *x-t* plots show the fluorescence intensity of Cal520LA-RBP (green) and TAMRA-RBP (red) as a function of distance (vertical axis) and time (horizontal axis) at (**Ba**) ribbon sites and (**Bb**) non-ribbon (NR) locations. The darker region at the upper edge of each plot is the extracellular space and the arrowheads show the timing of depolarization. Scale bars: vertical, 1.6 μm and horizontal, 75 ms.

C. Spatially averaged Cal520LA-RBP as a function of time at ribbon proximal (red), distal (blue), and non-ribbon locations (purple) n=26 (proximal ribbons), 26 (distal ribbons), and 15 (non-ribbon) from 5~8 different bipolar cells.

C *inset*. Temporal profile of events between 0-100 ms were expanded for better visualization. Scale bars: vertical, 0.2 μm ($\Delta F/F_{rest}$); horizontal, 20 ms.

D. Ca^{2+} measurements along the ribbon axis using the nanophysiology approach demonstrate the proximal Ca^{2+} signals can go as high as 26.4 $\pm$ 3.1 μM (red, N=26) and distal as 15.6 $\pm$ 1.5 μM (blue, N=26), and non-ribbon 10.4 $\pm$ 0.4 (NR, purple, N=15) respectively, in response to 10 ms stimuli. Error bars show standard errors.

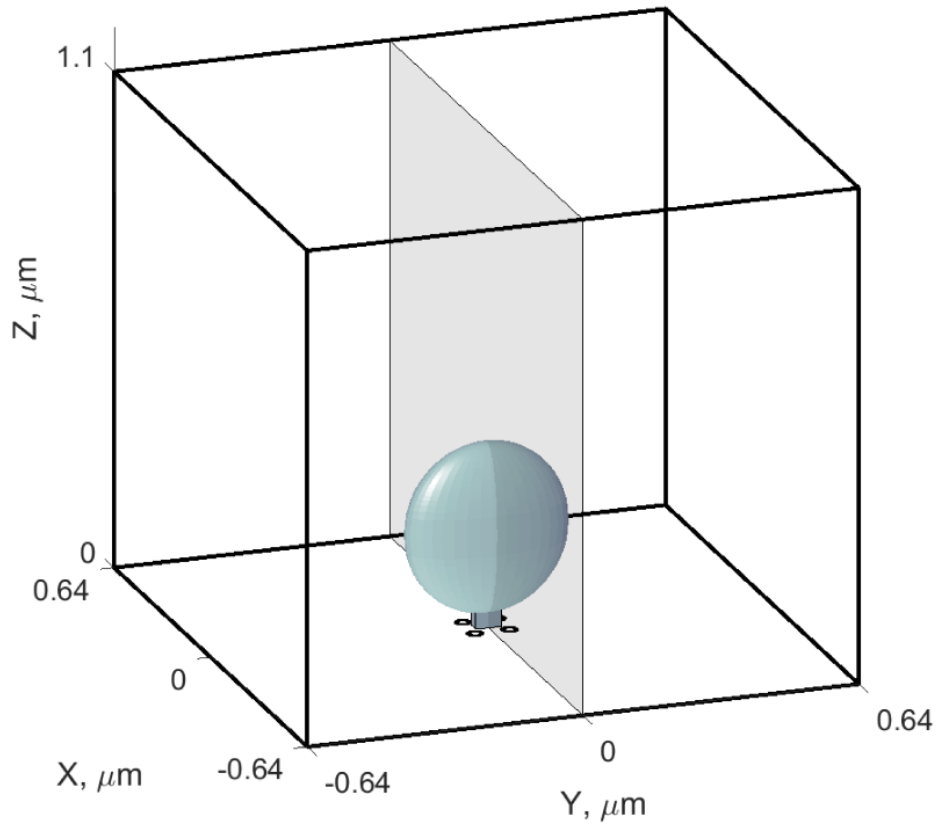

Fig. 6. Geometry of the computational model of intra-terminal Ca^{2+} dynamics.

Simulation domain is a box with dimensions (1.28 x 1.28 x 1.1) μm^3, approximating the fraction of synaptic terminal volume per single ribbon. Ca^{2+} ions enters near the base of the ellipsoidal ribbon at four locations marked by black disks representing Ca^{2+} channels or their clusters. The semi-transparent gray coordinate plane Y=0 corresponds to the section used for the pseudo-color 2D [Ca^{2+}] plots in **Figure 7**. Ca^{2+} is extruded on all surfaces of this domain, simulating combined clearance by pumps and exchangers on the plasmalemmal as well as internal endoplasmic reticulum and mitochondrial membranes.

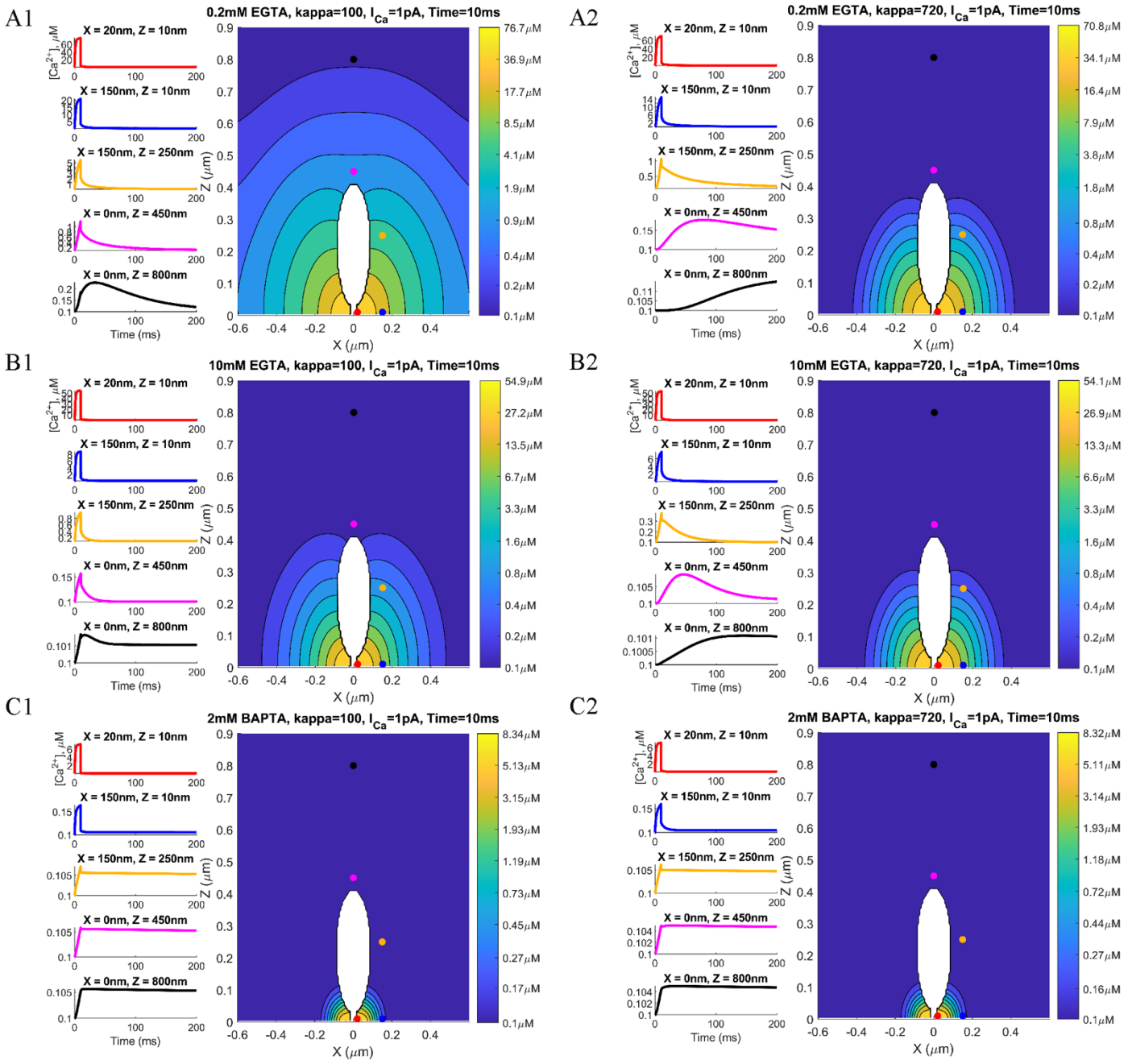

Fig.7 Simulation of the effect of an endogenous immobile buffer of different concentrations on [Ca^{2+}] dynamics in response to a 10ms pulse.

(**A1-C2**) In each sub-plot, the left-hand panels show the [Ca^{2+}] time course in response to a 10 ms constant current pulse (total current of 1 pA) at five select locations marked by colored circles in the right panel. The right-hand panels show a pseudo-color plot of [Ca^{2+}] in a 2D section of the 3D simulation volume in **Fig. 6**, at a fixed point in time corresponding to the end of the current pulse. Concentration values for each level curve are indicated in the color bar. Endogenous buffer is immobile, with a concentration of 200 μM in **panels A1-C1** (resting buffering capacity 100 μM), vs. 1.44 mM in **panels A2-C2** (resting buffering capacity 720). Exogenous buffer concentrations were 0.2 mM EGTA (**panels A1, A2**), 10 mM EGTA (**panels B1, B2**), 2 mM BAPTA (**panels C1, C2**).

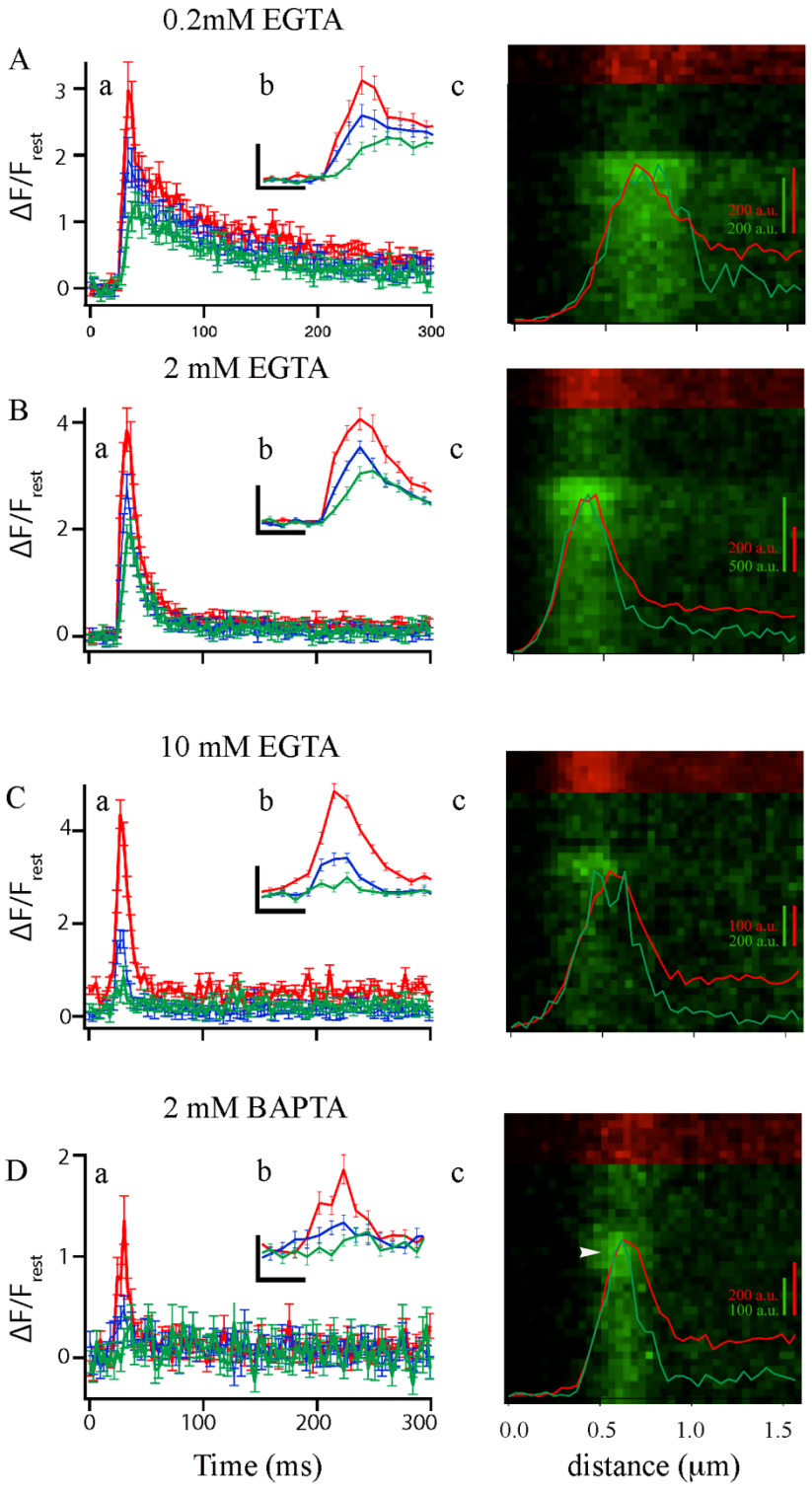

Fig.8. Spatiotemporal properties of Ca^{2+} microdomains in rod bipolar cell terminal recorded with high-affinity ribbon-bound dye.

Aa-Da. Average temporal fluorescence intensity (normalized to $\Delta F/F_{rest}$) of proximal (red), distal (blue), and cytoplasmic (green) Ca^{2+} signals with Cal520H-RBP as a function of time for distinct ribbon locations with pipette solution containing (**A**) 0.2 mM EGTA, (**B**) 2 mM EGTA, (**C**) 10 mM EGTA, or (**D**) 2 mM BAPTA.

Ab-Db. The temporal profile of events between 0-100 ms was expanded for better visualization. Scale bars: vertical, 0.5 ($\Delta F/F_{rest}$); horizontal, 20 ms.

Ac-Dc. Representative x-t images of the horizontal fluorescence intensity profiles show the Ca^{2+} signals obtained with Cal520H-RBP (green) and the ribbon location labeled with TAMRA-RBP (red), during depolarization on the x-axes.

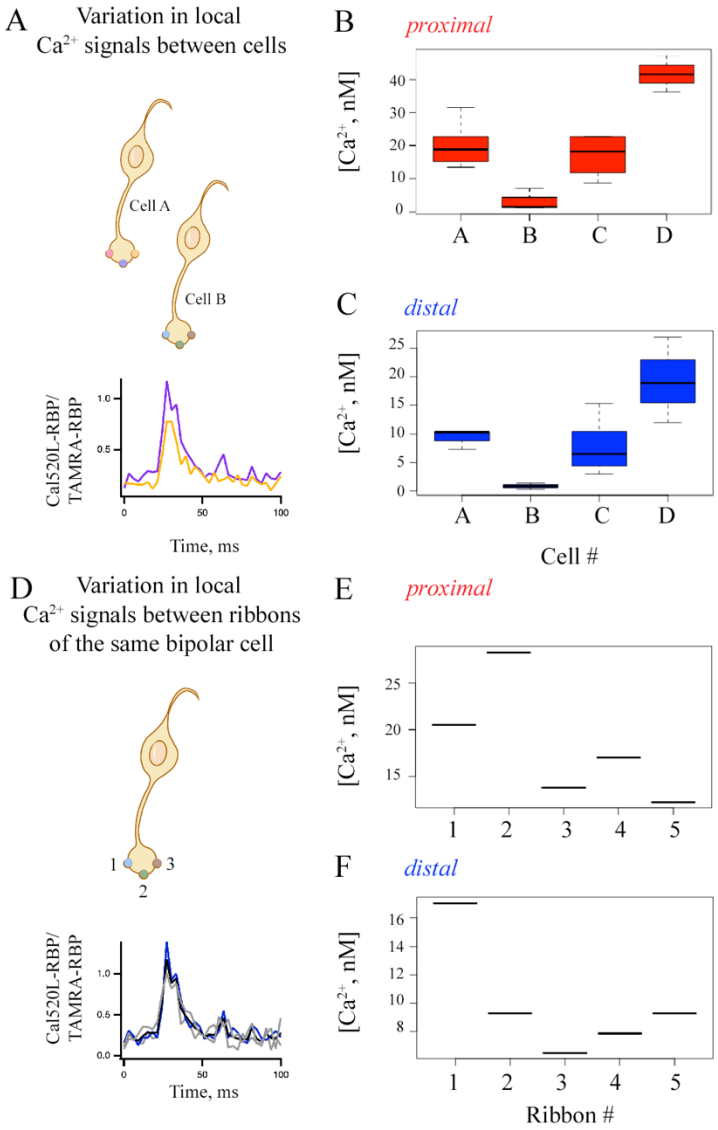

Fig.9. Heterogeneity in the spatiotemporal properties of Ca^{2+} microdomains in rod bipolar cell terminal.

A. Top panel. Cartoon of two representative rod BPCs (cell A and cell B), each containing differently colored ribbons. **Bottom panel.** Ribbon-to-ribbon variability was measured by recording local Ca^{2+} signals near different ribbons (yellow and purple traces) for each rod BPC. If a cell had multiple readings for a single ribbon, averages were obtained for comparisons as described in **Supplementary Fig. 9**.

B-C. Variability of Ca^{2+} signals in different ribbons across different cells in the presence of 10 mM EGTA, recorded using Cal520LA-RBP. Proximal Ca^{2+} amplitude values were significantly different between cells A and B ($p = 0.022$), cells A and D ($p = 0.023$), and cells B and D ($p = 0.005$) but similar between A and C (n = 4 cells, 4 fish). (**C**) In distal locations, ribbon amplitude values were significantly different between cells A and B ($p = 0.031$), but similar across all other cell comparisons (n = 4 cells, 4 fish).

D. Top panel. Illustration of a rod bipolar cell containing three ribbons (numbered 1-3). **Bottom panel.** Ca^{2+} signal measurements from three distinct ribbons (black, gray, and blue traces) were compared to determine the ribbon-to-ribbon variability within each bipolar cell as described in **Supplementary Fig. 10**.

E-F. Box plot illustrating $[Ca^{2+}]$ across various ribbons of an individual rod BPC. Ribbon variability within individual cells was measured with 10 mM EGTA using Cal520LA-RBP at (**E**) proximal and (**F**) distal locations. (**E**) Proximal Ca^{2+} amplitude values were significantly different among all ribbons ($p < 0.001$) (n = 5 ribbons, 1 rod BPCs, 1 fish). (**F**) Distal Ca^{2+} amplitudes were significantly different among all ribbon comparisons ($p < 0.001$) except for ribbons 2 and 5 (n = 5 ribbons, 1 rod BPCs, 1 fish). Similar analyses were conducted in two more cells and found similar observations (data not shown).

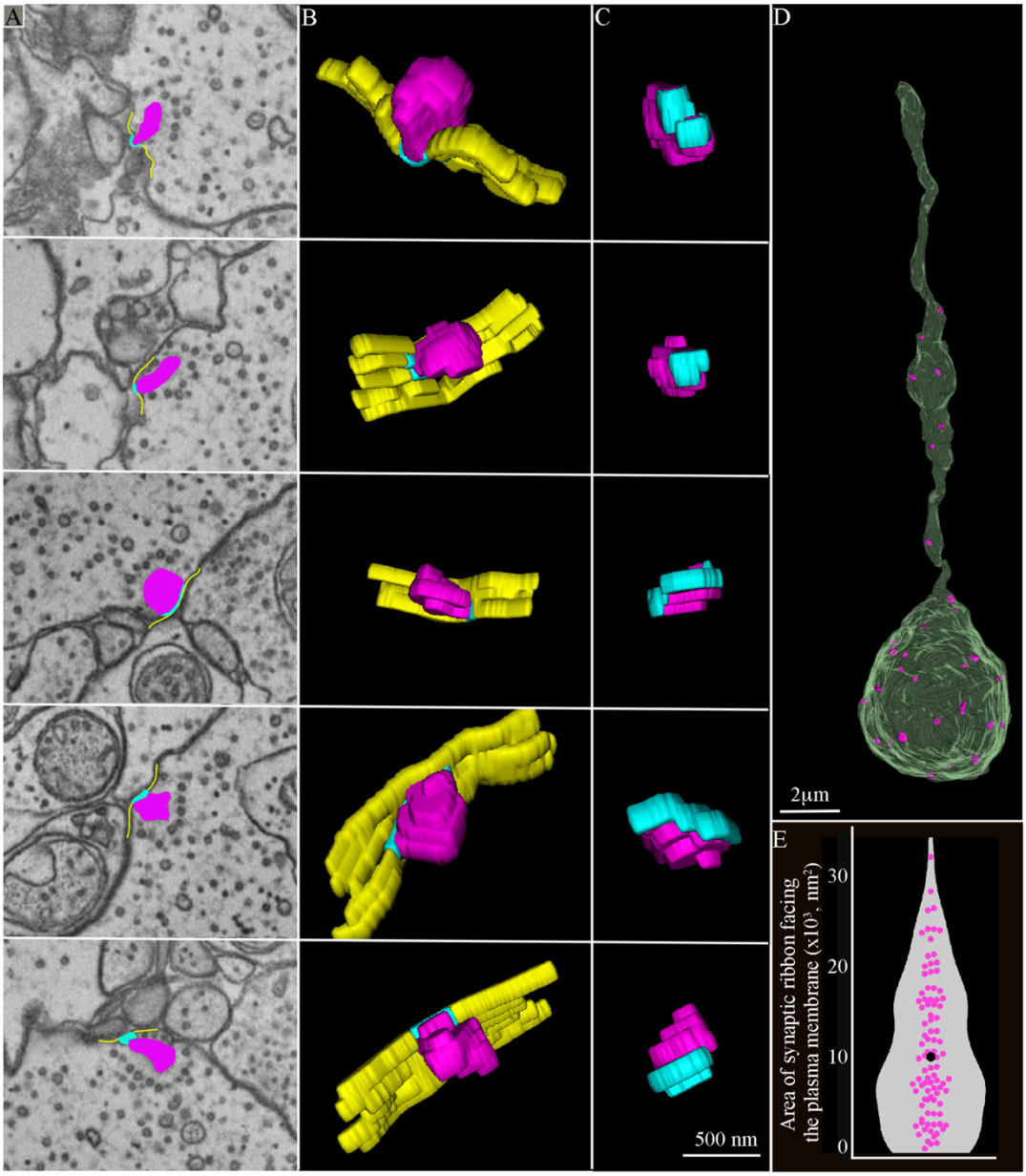

Fig. 10. Serial block-face scanning electron microscopy (SBF-SEM) analysis reveals heterogenous ribbon shape, size, and the area of the ribbon facing the plasma membrane where Ca^{2+} channels are located.

A-C. EM images of ribbon structures (**A**) and their respective 3D reconstructions to illustrate different shapes and sizes of synaptic ribbons (**A, B,** and **C**, magenta), plasma membrane (**A** and **B**, yellow), and the area of the ribbon facing the plasma membrane (**A, B,** and **C**, cyan). Each of the 5 rows of images illustrates one ribbon synapse from a zebrafish retinal rod bipolar cell.

D. Reconstruction of the rod bipolar cell terminal closest to the ganglion cell layer resembles the shape and the size of the mammalian rod bipolar cell RBC1 [2]. The ribbons are colored pink.

E. Summary of the area of the ribbon associated with the plasma membrane measured in the serial section of three-rod BPCs. The distribution of individual bipolar cells is shown in **Supplementary Fig. 10**. The z-size of the SBF-SEM sections is 50 nm, and each ribbon spans 2-5 consecutive sections. The solid pink circles in the violin plots show individual synaptic ribbon measurements from three rod bipolar cells, with the average measurements shown in the solid black circle.

References:

1. Vaithianathan, T., Henry, D., Akmentin, W., and Matthews, G. (2016). Nanoscale dynamics of synaptic vesicle trafficking and fusion at the presynaptic active zone. Elife *5*. 10.7554/eLife.13245.
2. Hellevik, A.M., Mardoum, P., Hahn, J., Kölsch, Y., D'Orazi, F.D., Suzuki, S.C., Godinho, L., Lawrence, O., Rieke, F., Shekhar, K., et al. (2024). Ancient origin of the rod bipolar cell pathway in the vertebrate retina. Nat Ecol Evol *8*, 1165-1179. 10.1038/s41559-024-02404-w.